

REVIEW

Optical Spatial Shock Waves in Nonlocal Nonlinear Media

Giulia Marcucci^{a,b}, Davide Pierangeli^{b,a}, Silvia Gentilini^{b,a}, Neda Ghofraniha^{b,a},
Zhigang Chen^{c,d} and Claudio Conti^{b,a,c}

^aDepartment of Physics, Sapienza University, Piazzale Aldo Moro 5, 00185 Rome, Italy;

^bInstitute for Complex Systems, National Research Council, Via dei Taurini 19, 00185 Rome, Italy; ^cThe Key Laboratory of Weak-Light Nonlinear Photonics, TEDA Applied Physics

Institute, Nankai University, Tianjin 300457, China; ^dDepartment of Physics and Astronomy, San Francisco State University, San Francisco, California 94132, USA.

ARTICLE HISTORY

Compiled December 21, 2024

ABSTRACT

Dispersive shock waves are fascinating phenomena occurring when nonlinearity overwhelms linear effects, such as dispersion and diffraction. Many features of shock waves are still under investigation, as the interplay with noninstantaneity in temporal pulses transmission and nonlocality in spatial beams propagation.

Despite the rich and vast literature on nonlinear waves in optical Kerr media, spatial dispersive shock waves in nonlocal materials deserve further attention for their unconventional properties. Indeed, they have been investigated in colloidal matter, chemical physics and biophotonics, for sensing and control of extreme phenomena.

Here we review the last developed theoretical models and recent optical experiments on spatial dispersive shock waves in nonlocal media. Moreover, we discuss observations in novel versatile materials relevant for soft matter and biology.

1. Introduction

Dispersive shock waves (DSWs) are rapidly oscillating solutions of hyperbolic partial differential equations that contrast the generation of multivalued regions through the formation of undular bores [1–11]. This class of phenomena was investigated in several physical fields, initially in shallow water waves [12] and ion-acoustic waves [13], then in oceanography [14], pulses propagation in photonic fibers [15,16], Bose-Einstein condensates [17–22], quantum liquids [23], photorefractive media [24], plasma physics [25], viscous fluids [26], and diffracting optical beams [5,27–40].

In 1967 Gardner, Greene, Kruskal and Miura developed a method to solve the Korteweg-de Vries (KdV) equation, called inverse scattering transform (IST) [41]. Among all the equations solvable by IST, which allowed to find the mathematical formulation of exact solutions of such nonlinear models, KdV and the nonlinear Schrödinger equation (NLSE) belong to the case with dispersive regularization of the aforementioned multivalued singularity. NLSE is a universal model that describes many phenomena, in particular a third-order nonlinear phenomenon in optics: the Kerr effect [42], a refractive index perturbation linearly scaling with the light inten-

sity. Kerr effect can be generalized to the nonlocal case when the nonlinear response in a specific point depends on entire beam transverse profile. This occurs, e.g., in thermal media [4,27,32,43–55]. In these materials, light propagation is affected by a highly nonlocal Kerr nonlinearity, ruled by nonlocal NLSE.

Unfortunately, IST is useless for the nonlocal NLSE and other theoretical approaches must be conceived. For many years, Whitham modulation and hydrodynamic approximation have predominated in solving the nonlocal NLSE [2,27]. However, hydrodynamic approximation cannot describe light propagating beyond the shock point, and two new techniques have been developed, one coming from nuclear physics, the time asymmetric quantum mechanics (TAQM) [11,56–66], which models the nonlinear wave intrinsically irreversible propagation as a superposition of decaying resonances, and the wave turbulence theory [31,37,39,67–69], which uses a statistical interpretation of nonlinear optics.

This review aims to summarize all the current theoretical models to describe wave breaking of nonlocal NLSE solutions in diffracting optical beam propagation, and to highlight some of the most recent experimental observations of DSWs in spatial nonlinear photonics.

After an introductory section about the derivation of nonlocal NLSE in Sec. 2, we report the main theoretical approaches and results related to DSWs. Section 2.1 explains in details the difference between the wave breaking due to local Kerr effect, which causes shock both in phase and in intensity, and the one in nonlocal Kerr media, where the beam intensity follows the phase singularity adiabatically [27]. The most recent theoretical models of nonlinear wave propagation in highly nonlocal nonlinear media are treated in Secs. 2.2, 2.3. Section 2.2 treats DSWs generated by laser beams and gives an analytical description of their intrinsic irreversibility, due to the complexity of the dynamics rather than losses [11]. Section 2.3 illustrates the importance of nonlocality in random dispersive waves nonlinear interaction to produce giant collective incoherent shock waves [37,39,69].

The second part of the manuscript is a collection of experiments on DSW generation in thermal media. Sec. 3 reports observations in Rhodamine solutions [27]. Output beam intensity profiles in Sec. 3.1 are modeled by TAQM both in two dimensional experiments, where decaying states describe the longitudinal propagation [35,36], and in the one dimensional approximation, having the proof that TAQM is an excellent approach also to analyze transverse intensity profiles beyond the shock point [38]. The interplay of nonlinearity and disorder is illustrated in Sec. 3.2. There, observations in Rhodamine with silica spheres [30] and in silica aerogel [33] exhibit the competition between randomness and nonlocal Kerr effect. DSW generation processes in chemical [34] and biological solutions [40] are illustrated in Sec. 3.3. Last but not least, Sec. 3.4 shows recent experiments on the transition from coherent shocklets to a giant incoherent DSW in a photon fluid, modeled by wave turbulence theory [37].

2. The Nonlocal Nonlinear Schrödinger Equation

From Maxwell’s equations, considering a region with zero charge, current and magnetization, we obtain the following electric field wave equation

$$-\nabla^2 \mathbf{E} + \frac{1}{c^2} \partial_t^2 \mathbf{E} = -\frac{1}{\epsilon_0 c^2} \partial_t^2 \mathbf{P}, \quad (1)$$

with \mathbf{E} the electric field and \mathbf{P} the medium nonlinear polarization [70].

The relation between \mathbf{P} and \mathbf{E} depends on the material properties. Including all the nonlinear terms, we have

$$\mathbf{P} = \epsilon_0 \left(\chi^{(1)} \mathbf{E} + \chi^{(2)} \mathbf{E}\mathbf{E} + \chi^{(3)} \mathbf{E}\mathbf{E}\mathbf{E} + \dots \right) = \mathbf{P}^{(L)} + \mathbf{P}^{(NL)}, \quad (2)$$

where $1 + \chi^{(1)} = n_0^2$, n_0 is the medium refractive index, $\chi^{(2)}$ and $\chi^{(3)}$ are tensors denoted as second and third order susceptibility, respectively.

One must take into account the temporal delay between the instant when the electric field reaches the medium and the medium response. For this reason, this radiation-matter interaction is more properly represented by the following non instantaneous superposition of linear and nonlinear polarization [70]:

$$\mathbf{P} = \epsilon_0 \left(\chi^{(1)} * \mathbf{E}(t) + \chi^{(2)} * \mathbf{E}\mathbf{E}(t) + \chi^{(3)} * \mathbf{E}\mathbf{E}\mathbf{E}(t) + \dots \right) = \mathbf{P}^{(L)} + \mathbf{P}^{(NL)}, \quad (3)$$

where $*$ is the convolution product

$$\chi^{(n)} * \mathbf{E} \dots \mathbf{E}(t) = \int_{-\infty}^t dt_1 \int_{-\infty}^{t_1} dt_2 \dots \int_{-\infty}^{t_{n-1}} dt_n \chi^{(n)}(t - t_1, \dots) \mathbf{E}(\mathbf{R}, t_1) \dots \mathbf{E}(\mathbf{R}, t_n).$$

If we have a third-order isotropic and centrosymmetric material, the nonlinear polarization is

$$\mathbf{P}^{(NL)}(\mathbf{R}, t) = \epsilon_0 \int_{-\infty}^t dt_1 \int_{-\infty}^{t_1} dt_2 \int_{-\infty}^{t_2} dt_3 \chi^{(3)}(t - t_1, t - t_2, t - t_3) \mathbf{E}(\mathbf{R}, t_1) \mathbf{E}(\mathbf{R}, t_2) \mathbf{E}(\mathbf{R}, t_3) \quad (4)$$

and the related dielectric tensor changes as

$$\epsilon_{new} = \epsilon + \epsilon_2 \langle \mathbf{E} \cdot \mathbf{E} \rangle, \quad (5)$$

where $\langle \mathbf{E} \cdot \mathbf{E} \rangle = \frac{1}{2} |\mathbf{E}|^2$ is the square of the electric field time average. The final refractive index causes the Kerr effect [70], a phenomenon that consists in a perturbation of the medium refractive index, proportional to the field intensity:

$$n = \sqrt{\epsilon_{new}} = \sqrt{\epsilon + \epsilon_2 \langle \mathbf{E} \cdot \mathbf{E} \rangle} \approx n_0 + n_2 I, \quad (6)$$

with $I = |\mathbf{E}|^2$ the field intensity and n_2 the Kerr coefficient.

The nonlocal Kerr effect is a third order phenomenon, but the radiation-matter interaction depends on the whole transverse intensity profile, as occurs in thermal media. In these materials, when an optical beam propagates, it locally heats the medium and the resulting temperature gradient generates a variation of the density distribution, and a refractive index perturbation [27]:

$$\Delta n = \left(\frac{\partial n}{\partial T} \right)_0 \Delta T. \quad (7)$$

The beam acts like a heat source and, in a stationary limit and low absorption approximation, the temperature variation around the beam center is governed by the

following heat equation [27,43,48,49,71,72]

$$(\partial_X^2 + \partial_Y^2) \Delta T - L_{nloc}^{-2} \Delta T = -\gamma |\mathbf{E}(\mathbf{R})|^2, \quad (8)$$

where $\gamma = (L_{loss} \rho_0 c_P D_T)^{-1}$, L_{loss} is the loss characteristic length, ρ_0 is the material density, c_P is the specific heat at constant pressure, D_T is the thermal diffusivity, $L_{nloc} = \sqrt{\frac{|n_2|}{\gamma |\frac{\partial n}{\partial T}|_0}}$ is the nonlocality length, which expresses the width of the refractive index perturbation, and $\mathbf{R} = (X, Y, Z) = (\mathbf{R}_\perp, Z)$. The solution can be written as

$$\Delta T(\mathbf{R}) = \int d\mathbf{R}_\perp' G(\mathbf{R}_\perp - \mathbf{R}_\perp') |\mathbf{E}(\mathbf{R}_\perp', Z)|^2, \quad (9)$$

with $G(\mathbf{R}_\perp' - \mathbf{R}_\perp')$ the heat equation Green function. Equation (9) depends on the boundary conditions and proves the nonlocality of this nonlinear effect. From Eq. (9) we obtain

$$\Delta n[I](\mathbf{R}) = n_2 \int d\mathbf{R}_\perp' K(\mathbf{R}_\perp - \mathbf{R}_\perp') I(\mathbf{R}_\perp', Z), \quad (10)$$

whence

$$n[I](\mathbf{R}) = n_0 + n_2 \int d\mathbf{R}_\perp' K(\mathbf{R}_\perp - \mathbf{R}_\perp') I(\mathbf{R}_\perp', Z), \quad (11)$$

with $n_2 K(\mathbf{R}_\perp) = \left(\frac{\partial n}{\partial T}\right)_0 G(\mathbf{R}_\perp)$. By a comparison between the nonlocality length L_{nloc} and the beam waist W_0 , we can analyze two different limits: the standard Kerr effect in Eq. (6) when $L_{nloc} \ll W_0$ (local approximation), i.e., $K(\mathbf{R}_\perp - \mathbf{R}_\perp') \sim \delta(\mathbf{R}_\perp - \mathbf{R}_\perp')$, and the opposite case $L_{nloc} \gg W_0$, that is, the highly nonlocal approximation (HNA), where $K * I(\mathbf{R}) \sim K(\mathbf{R}_\perp) P(Z)$, with $P(Z) = \int d\mathbf{R}_\perp I(\mathbf{R})$ the power.

For a monochromatic field $\mathbf{E}(\mathbf{R}, \tau) = \hat{\mathbf{E}}_0 A(\mathbf{R}) e^{-i\omega\tau}$ in a third-order thermal medium, in paraxial and slowly varying envelope approximations, introducing the delayed time $\tau = t - \frac{n_0}{c} Z$ and adding a linear loss of characteristic length L_{loss} , from Eq. (1) we find that the propagation along Z is ruled by the nonlocal NLSE [27]:

$$2ik\partial_Z A + (\partial_X^2 + \partial_Y^2) A + 2k^2 \frac{\Delta n[|A|^2](\mathbf{R})}{n_0} A = -i \frac{k}{L_{loss}} A, \quad (12)$$

with $k = \frac{2\pi n_0}{\lambda} = \frac{\omega n_0}{c}$ the wavenumber.

2.1. Spatial Dispersive Shock Waves in Nonlocal Kerr Nonlinearity

Spatial DSWs are rapidly oscillating waves which regularize an abrupt discontinuity in phase through diffraction, that is, through the formation of intensity undular bores on the beam borders. Scientific community paid close attention to the theoretical description [1,2,21] and experimental demonstration [13,15,17–20,25–28,31] of optical DSWs. Here we summarize results on the defocusing DSWs in nonlocal media [27]. In such materials, the IST cannot describe the solutions, and we need other methods.

In next two sections, we detail two different methodologies for DSWs in nonlocal media: the TAQM [11,56–66] and the wave turbulence theory [67,69]. Both theories also prove that DSWs are intrinsically irreversible.

Starting from Eq. (12), through the scaling $x = \frac{X}{W_0}$, $y = \frac{Y}{W_0}$, $z = \frac{Z}{L}$, $\psi(x, y, z) = \frac{A(X, Y, Z)}{\sqrt{I_0}}$, with I_0 the intensity peak, $L = \sqrt{L_{nl}L_d}$, $L_{nl} = \frac{n_0}{k|n_2|I_0}$ the nonlinear length scale associated to a local Kerr effect, $L_d = kW_0^2$ the diffraction length, one obtains the normalized nonlocal NLSE

$$i\epsilon\partial_z\psi + \frac{\epsilon^2}{2}(\partial_x^2 + \partial_y^2)\psi + \chi\theta\psi = -i\frac{\alpha}{2}\epsilon\psi, \quad (13)$$

with $\epsilon = \frac{L_{nl}}{L} = \sqrt{\frac{L_{nl}}{L_d}}$ a small quantity in strongly nonlinear (or weakly diffracting) regime, as the one we are considering, $\chi = \frac{n_2}{|n_2|}$, $\theta = \left| \frac{k\Delta n L_{nl}}{n_0} \right|$, $\alpha = \frac{L}{L_{loss}}$. From Eq. (9)

$$-\sigma^2(\partial_x^2 + \partial_y^2)\theta + \theta = |\psi|^2, \quad (14)$$

where $\sigma = \frac{L_{nl,loc}}{W_0}$ is the nonlocality degree, which expresses the nature of the Kerr effect through the limits we have previously discussed: if $\sigma \ll 1$ we are considering the local limit $\theta \sim |\psi|^2$, instead, if $\sigma \gg 1$, by HNA $\theta \sim \kappa(x, y)p(z)$, with $p(z) = \int dx dy |\psi(x, y, z)|^2 = \frac{P(Z)}{W_0^2 I_0}$.

The fundamental laser mode (Gaussian TEM₀₀) is described by an axisymmetric Gaussian input $\psi_0(r) = \exp(-r^2)$, with $r = \sqrt{x^2 + y^2}$, which evolves in the WKB approximation [73] as $\psi(r, z) = \sqrt{\rho(r, z)} \exp\left[i\frac{\phi(r, z)}{\epsilon}\right]$. For $D = 2$ the transverse dimensionality and $u = \partial_r\phi$ the phase chirp, from Eqs. (13, 14) one obtains

$$\begin{aligned} \partial_z\rho + \left[\frac{D-1}{r}\rho u + \partial_r(\rho u)\right] &= -\alpha\rho, \\ \partial_z u + u\partial_r u - \chi\partial_r\theta &= 0, \\ -\sigma^2\left[\partial_r^2\theta + \frac{D-1}{r}\partial_r\theta\right] + \theta &= \rho. \end{aligned} \quad (15)$$

Figure 1 reports phase chirp and field amplitude for $D = 1$, so for $\partial_y \sim 0$ and $r \rightarrow x$, in a defocusing medium ($\chi = -1$) without losses ($\alpha = 0$). The local case ($\sigma = 0$) is illustrated in Figs. 1a,c and follows from system (15):

$$\partial_z\rho + \partial_x(\rho u) = 0, \quad \partial_z u + u\partial_x u = -\partial_x\rho. \quad (16)$$

Eqs. (16) are equivalent to Euler and continuity equations, respectively, for a fluid of speed u , mass density ρ and pressure proportional to ρ^2 . In the reported dynamics, the diffraction, initially of order ϵ^2 , starts to play a relevant role in proximity of the wave breaking. In fact, it regularizes such a discontinuity by rapid oscillations of wavelength $\sim \epsilon$, which appear simultaneously in phase chirp u and intensity ρ . For large values of σ , the normalized refractive index variation, here expressed by $\theta(x)$, is wider than the Gaussian input. As shown in Figs. 1b,d the shock oscillations are essentially driven by the phase chirp u , while the intensity ρ adiabatically follows. Major details are given in [27].

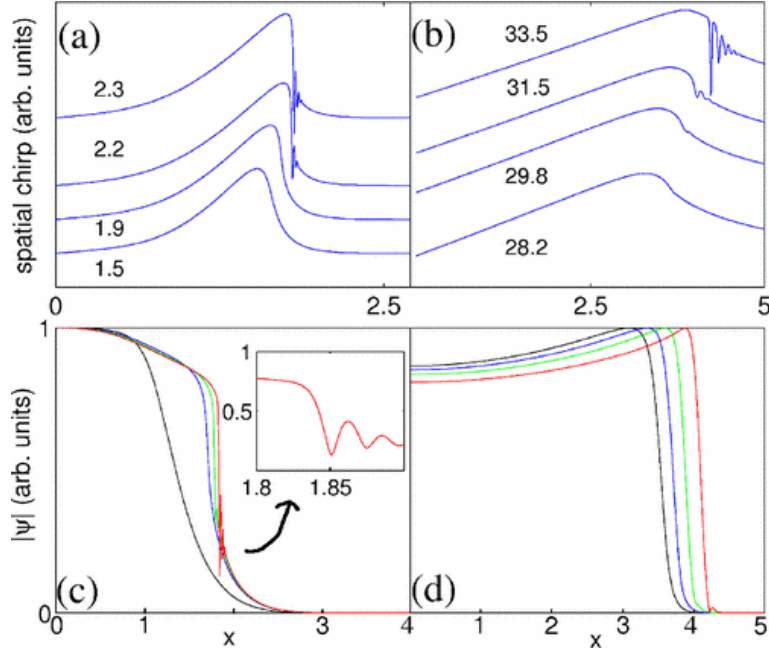


Figure 1. Phase chirp $u(x)$ (a,b), and amplitude $\sqrt{\rho(x,z)}$ (c,d) for transverse dimensionality $D = 1$ and different values of z , as indicated. (a,c) are obtained by Eqs. (16) with $\epsilon = 10^{-3}$. (b,d) are simulations of the result of the system (15) with $D = 1$, $\alpha = 0$, $\chi = -1$, $\sigma^2 = 5$.

FIG. 1 reprinted with permission from [27]. Copyright 2007 by the American Physical Society.

2.2. High Nonlocality and Time Asymmetric Quantum Mechanics

Let us consider the nonlocal NLSE in Eq. (12) with a medium response function $K(X, Y) = \exp[-(|X| + |Y|)/L_{nl}] / (2L_{nl})^2$. Being K separable, i.e., $K(X, Y) = \tilde{K}(X)\tilde{K}(Y)$, through the approximation $\partial_Y \sim 0$ (as in the previous section) we can consider only one transverse dimension, since analyzing propagation along Y is no more interesting for our purposes. We rewrite Eq. (12) in terms of 1 + 1 dimensionless variables by using the same scaling of Eq. (13) and choosing I_0 such that $L_{nl} = L_d$:

$$i\partial_z\psi + \frac{1}{2}\partial_x^2\psi - \kappa * |\psi|^2\psi = -i\frac{\alpha}{2}\psi. \quad (17)$$

with $\kappa(x) = W_0\tilde{K}(xW_0) = \exp(-|x|/\sigma)/(2\sigma)$.

We take into account a medium where the nonlocality length is much larger than the beam waist. By HNA we have [51,74]

$$\kappa * |\psi|^2 \sim \kappa(x)p(z), \quad (18)$$

where κ is a function no more depending on $|\psi|^2$. In a system without loss, that is, $\alpha = 0$, the normalized power p is conserved and the NLSE is mapped into a linear Schrödinger equation $i\partial_z\psi = \hat{H}\psi$, with the Hamiltonian $\hat{H} = \frac{1}{2}\hat{p}^2 + p\kappa(x)$ ($\hat{p} = -i\partial_x$). When we express the even function κ as its second order expansion, that is, $\kappa(x) = \kappa_0^2 - \frac{\kappa_2^2}{2}x^2$, where $\kappa_0^2 = \frac{1}{2\sigma}$ and $\kappa_2^2 = \frac{1}{\sqrt{\pi}\sigma^2}$, we obtain the reversed harmonic

oscillator (RHO) Hamiltonian [61,63,66]:

$$\hat{H} = p\kappa_0^2 + \hat{H}_{RHO}, \quad \hat{H}_{RHO} = \frac{\hat{p}^2}{2} - \frac{\gamma^2 \hat{x}^2}{2}, \quad \gamma^2 = p\kappa_2^2. \quad (19)$$

If $\psi = \exp(-i\kappa_0^2 pz) \phi$, then $i\partial_z \phi = \hat{H}_{RHO} \phi$.

Figure 2 sketches the relation between the harmonic and the reversed oscillators. For a harmonic oscillator (HO), the spectrum is discrete and the corresponding eigenstates form a orthonormal basis (both a orthogonality and a completeness relations hold):

$$\begin{aligned} \hat{H}_{HO} &= \frac{\hat{p}^2}{2} + \frac{\omega^2}{2} \hat{x}^2 \\ \hat{H}_{HO} \psi(x) &= E \psi(x), \quad E_n = \omega \left(n + \frac{1}{2}\right), \\ \psi_n(x) &= \sqrt{\frac{\omega}{\pi}} \frac{1}{\sqrt{2^n n!}} H_n(\sqrt{\omega} x), \end{aligned} \quad (20)$$

with $H_n(x) = (-1)^n x^2 \frac{d^n}{dx^n} e^{-x^2}$ the Hermite polynomials. On the other hand, RHO has complete continuous spectrum, but one derives a generalized discrete spectrum from HO spectrum by a complex analytic prolongation in the rigged Hilbert space [60,66,75] through the transformation $\omega \rightarrow i\gamma$, $\hat{x} \rightarrow e^{-i\frac{\pi}{4}} \hat{x}$, $\hat{p} \rightarrow e^{i\frac{\pi}{4}} \hat{p}$ [63,66]. The new stationary Schrödinger equation is $\hat{H}_{RHO} \mathfrak{f}_n^\pm(x) = \frac{\Gamma}{2} \mathfrak{f}_n^\pm(x)$, solved by the spectrum $\frac{\Gamma_n}{2} = i\gamma \left(n + \frac{1}{2}\right)$ and the non normalizable eigenfunctions

$$\mathfrak{f}_n^\pm(x) = \frac{\sqrt[4]{\pm i\gamma}}{\sqrt{2^n n!} \sqrt{\pi}} H_n(\sqrt{\pm i\gamma} x) \exp(\mp i \frac{\gamma}{2} x^2), \quad (21)$$

namely, the RHO *Gamow vectors* (GVs) [76,77].

We can express every wavefunction as a truncated superposition of GVs added to a background function, which dispersively oscillates at infinite as a polynomials [66]:

$$\phi(x) = \phi_N^G(x) + \phi_N^{BG}(x) \quad (22)$$

with

$$\phi_N^G(x) = \sum_{n=0}^N \mathfrak{f}_n^-(x) \langle \mathfrak{f}_n^+ | \phi(x, 0) \rangle. \quad (23)$$

Figure 3 shows the GV square norms (Fig. 3a) and phase chirps (Fig. 3b). The evolution of the normalized field ψ presents a Gamow part resulting as a superposition of exponential decays with quantized decay rates [66]:

$$\psi_n^G(x, z) = \sum_{n=0}^N \langle \mathfrak{f}_n^+ | \psi(x, 0) \rangle \mathfrak{f}_n^-(x) e^{-i\kappa_0^2 pz} e^{-\frac{\Gamma_n}{2} z}. \quad (24)$$

Eq. (24) proves an intrinsical irreversibility of DSWs, where a backward propagation beyond the shock point is no physically possible because of the exponentially decaying evolution. This explains why the quantum representation of wave propagation theory in a rigged Hilbert space is called TAQM (here time is replaced by z).

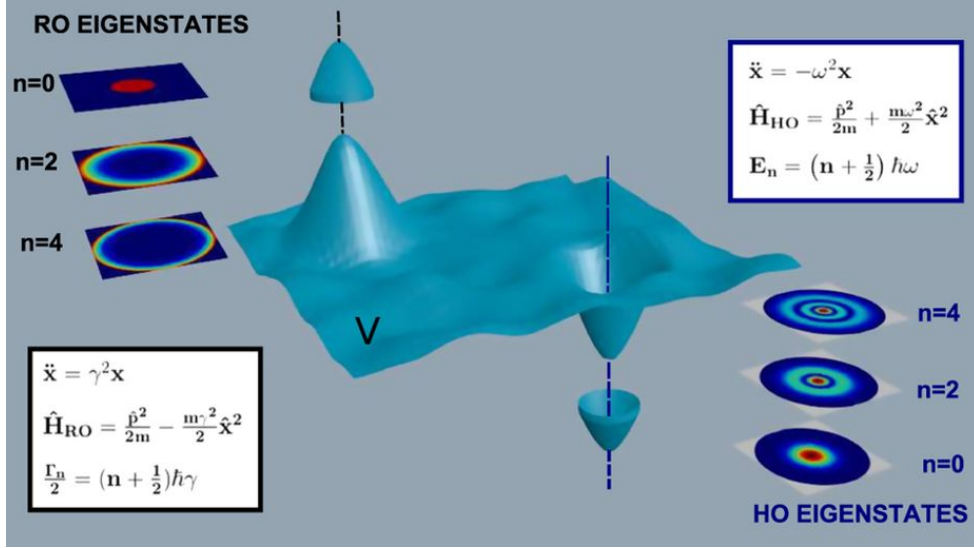


Figure 2. Pictorial representation of an energy landscape. When the system is in proximity of a local maximum it obeys the RHO Hamiltonian, in figure \hat{H}_{RO} . In proximity of the minimum the system obeys the Hamiltonian of a harmonic oscillator, in figure \hat{H}_{HO} . The two Hamiltonians are explicitly written in the two the corresponding text boxes, with the related dynamical systems and the discrete eigenvalues. Insets show the transverse profiles of the respective eigenfunctions, bounded on right hand side for the harmonic oscillator, unbounded on the left hand side for the RHO.

Reprinted by permission from Macmillan Publishers Ltd. from [36]. Copyright 2015.

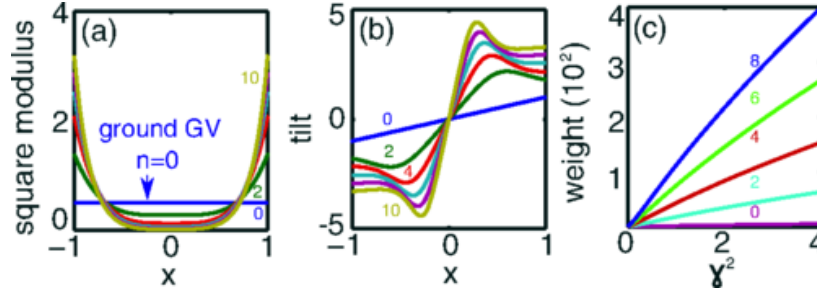


Figure 3. (a) $||f_n^-(x)||^2$ in Eq. (21) for increasing even order n ; (b) corresponding phase chirps $\partial_x \text{Arg} [f_n^-(x)]$; (c) weights $p_n(0)$ [Eq. (25)] of the GV expansion of a Gaussian wave packet.

FIG. 1 reprinted with permission from [35]. Copyright 2015 by the American Physical Society.

In the probabilistic interpretation of TAQM [35], the projection of Eq. (24) over $\sqrt{\Gamma_n} f_n^+$ gives the probability $p_n(z)$ of finding the system in a decaying GV

$$p_n(z) = \Gamma_n |\langle f_n^+ | \psi(x, 0) \rangle|^2 e^{-\Gamma_n z}, \quad (25)$$

which gives the z -dependent weight of the n -order GV. Initial weights $p_n(0)$ are reported in Fig. 3c as functions of γ^2 . Since a Gaussian beam $\psi(x, 0) = \varphi(x) = \exp(-x^2/2)/\sqrt{\pi}$ is an even input, all the odd terms in Eq. (24) vanish due the x -parity. Figure 4a shows the numerical solution of Eq. (17). Yellow lines give the transverse intensity profile. We see that these are modeled by a superposition of exponential decays, where the plateau is given by the groundstate GV, and the peaks are given by higher order GVs. Simulations of weights $p_n(z)$ are in Figs. 4b,c. While dotted profiles are numerical results from Eq. (25), continuous lines result from the general projection

definition $p_n(z) = \Gamma_n |\langle f_n^+ | \psi(x, z) \rangle|^2$, with $\psi(x, z)$ numerical solution of Eq. (17).

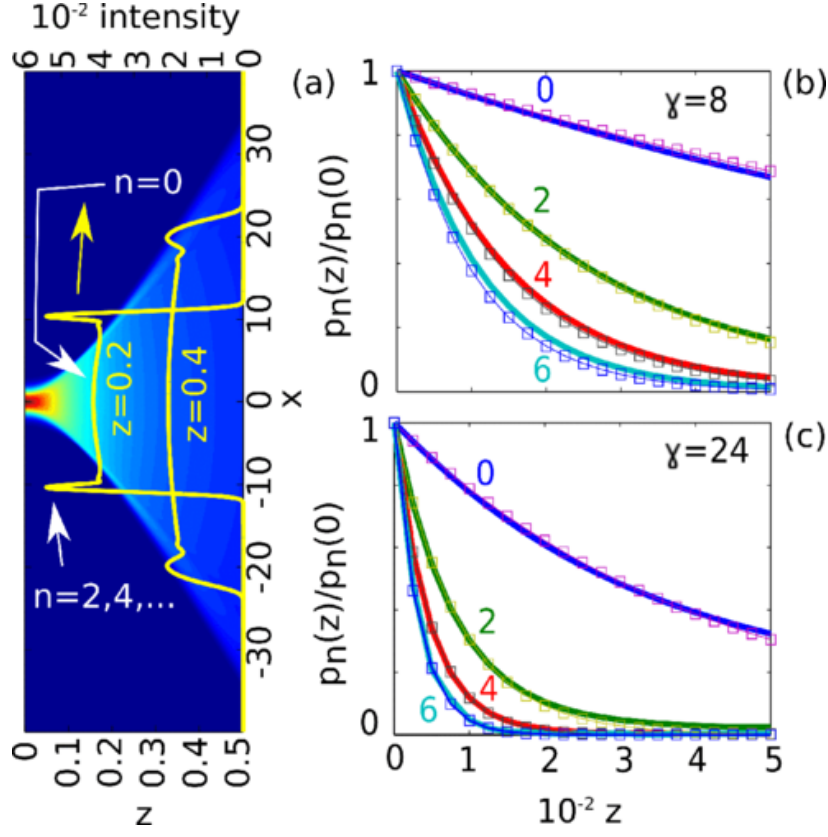


Figure 4. (a) Numerical solution of Eq. (17) with $p = 10^4$ and $\sigma^2 = 10$; (b) projection on GVs for increasing order n for $\alpha = 0.3$ and $\gamma = 8$; continuous lines are from Eq. (17), dots are from Eq. (25); (c) as in panel (b) for $\gamma = 24$.

FIG. 2 reprinted with permission from [35]. Copyright 2015 by the American Physical Society.

2.3. Random Optical Waves and Turbulence Theory

We have summarized how TAQM describes the intrinsic irreversibility of DSWs generated by a laser input. We highlight that nonlinear optics offers other examples of intrinsic irreversibility, as photon fluids, i.e., turbulent flows of a conservative systems of random optical waves, in which the statistical interpretation has produced significant results [69].

Statistical nonlinear optics is related to wave turbulence theory, whereby the kinetic wave description provides a thermodynamic treatment of turbulence [31,37,39,67–69,78–81]. If one considers the nonlinear propagation of incoherent optical waves characterized by fluctuations that are statistically inhomogeneous in space, DSWs arise only in the strong turbulence (strongly nonlinear) regime [37,39]. The wave breaking emerges from a turbulent field, whose local averaged spectrum follows a specific Vlasov-like kinetic equation, which can be a traditional Vlasov equation (local nonlinearity), a short-range Vlasov equation (SRVE) (quasi-local nonlinearity) or a long-range Vlasov equation (LRVE) (highly nonlocal nonlinearity), derived by the zero-loss NLSE through a multiscale expansion [69].

In what follows, we analyze long-range interactions in strongly nonlinear wave

systems operating far from thermodynamic equilibrium. Starting from the NLSE [Eq. (12)], with nonlinearity expressed by Eq. (10) and no loss, we obtain Eq. (13), here explicitly written as

$$i\partial_z\psi + \frac{\epsilon}{2}(\partial_x^2 + \partial_y^2)\psi + \chi v\psi U * |\psi|^2 = 0, \quad (26)$$

with $v = \frac{|n_2|I_0}{n_0}k\sqrt{L_{nl}L_d}$, $U(\mathbf{r}) = W_0^2 K(W_0\mathbf{r})$, $\mathbf{r} = (x, y)$. From Eq. (26), we want to attain a kinetic equation, that is, an equation describing the evolution of the spectrum during the related field propagation in the nonlinear medium. The structure of a kinetic equation depends on the statistics of the random wave. For this reason, we consider the field autocorrelation function

$$B(\mathbf{r}, \xi, z) = \langle \psi(\mathbf{r} + \frac{1}{2}\xi, z)\psi^*(\mathbf{r} - \frac{1}{2}\xi, z) \rangle, \quad \mathbf{r} = (\mathbf{r}_1 + \mathbf{r}_2)/2, \quad \xi = \mathbf{r}_1 - \mathbf{r}_2. \quad (27)$$

The statistics is said to be homogeneous if B depends only on the distance $|\mathbf{r}_1 - \mathbf{r}_2|$. Following Eq. (26)

$$i\partial_z B(\mathbf{r}, \xi, z) + \epsilon \nabla_{\mathbf{r}} \cdot \nabla_{\xi} B(\mathbf{r}, \xi, z) + \chi v [P(\mathbf{r}, \xi, z) - Q(\mathbf{r}, \xi, z)] = 0, \quad (28)$$

with

$$\begin{aligned} P(\mathbf{r}, \xi, z) &= B(\mathbf{r}, \xi, z) \int d\mathbf{r}' U(\mathbf{r}') [N(\mathbf{r} - \mathbf{r}' + \frac{1}{2}\xi, z) - N(\mathbf{r} - \mathbf{r}' - \frac{1}{2}\xi, z)], \\ Q(\mathbf{r}, \xi, z) &= \int d\mathbf{r}' U(\mathbf{r}') [B(\mathbf{r} - \frac{1}{2}\mathbf{r}' + \frac{1}{2}\xi, \mathbf{r}', z)B(\mathbf{r} - \frac{1}{2}\mathbf{r}', \xi - \mathbf{r}', z) + \\ &\quad - B(\mathbf{r} - \frac{1}{2}\mathbf{r}', \xi + \mathbf{r}', z)B(\mathbf{r} - \frac{1}{2}\mathbf{r}' - \frac{1}{2}\xi, -\mathbf{r}', z)], \\ N(\mathbf{r}, z) &= B(\mathbf{r}, \xi = \mathbf{0}, z) = \langle |\psi|^2 \rangle(\mathbf{f}, z). \end{aligned} \quad (29)$$

In the last equation, N is the averaged field power, also depending on \mathbf{r} because of the inhomogeneity of the statistics. By defining the length scale of random fluctuations as the coherence length λ_c and W_0 the incoherent beam waist, we can assume that the statistics is quasi-homogeneous if $\epsilon_c = \lambda_c/W_0 \ll 1$. For a Gaussian response function $U(\mathbf{r}) = \frac{1}{2\pi\sigma^2} \exp\left(-\frac{|\mathbf{r}|^2}{2\sigma^2}\right)$, we get the SRVE if $\sigma \ll 1$ and the LRVE if $\sigma \gg 1$ through two different multiscale expansion with respect to ϵ_c :

$$\partial_z n_{\mathbf{k}}(\mathbf{r}, z) + \nabla_{\mathbf{k}} \tilde{\omega}_{\mathbf{k}}(\mathbf{r}, z) \cdot \nabla_{\mathbf{r}} n_{\mathbf{k}}(\mathbf{r}, z) - \nabla_{\mathbf{r}} \tilde{\omega}_{\mathbf{k}}(\mathbf{r}, z) \cdot \nabla_{\mathbf{k}} n_{\mathbf{k}}(\mathbf{r}, z) = 0, \quad (30)$$

for the local spectrum $n_{\mathbf{k}}(\mathbf{r}, z) = \int d\xi B(\mathbf{r}, \xi, z) \exp(-i\mathbf{k} \cdot \xi)$, with averaged power $N(\mathbf{r}, z) = \frac{1}{(2\pi)^2} \int d\mathbf{k} n_{\mathbf{k}}(\mathbf{r}, z)$. The nonlocal features of Eq. (30) are traced by the generalized dispersion relation. Once defined the Fourier transform of the response function $\tilde{U}(\mathbf{k}) = \int d\mathbf{r} U(\mathbf{r}, z) \exp(-i\mathbf{k} \cdot \mathbf{r})$, for the LRTE

$$\begin{aligned} \tilde{\omega}_{\mathbf{k}}(\mathbf{r}, z) &= \omega(\mathbf{k}) + V(\mathbf{r}, z), \\ \omega(\mathbf{k}) &= \frac{\epsilon}{2} |\mathbf{k}|^2, \\ V(\mathbf{r}, z) &= -\chi v \int d\mathbf{r}' U(\mathbf{r} - \mathbf{r}') N(\mathbf{r}', z). \end{aligned} \quad (31)$$

One can also compute the momentum both from the NLSE and the LRVE:

$$\begin{aligned}\mathbf{p}_{NLSE}(\mathbf{r}, z) &= (2\pi)^2 \Im(\psi^* \nabla \psi) / N(\mathbf{r}, z), \\ \mathbf{p}_{LRVE}(\mathbf{r}, z) &= \int d\mathbf{k} n_{\mathbf{k}}(\mathbf{r}, z) \mathbf{k} / N(\mathbf{r}, z).\end{aligned}\tag{32}$$

Major details are given in [69].

By increasing the range of the nonlocality, we pass from a stage where the field evolution is ruled by stochastic generation of small-scale DSW structures, naturally denoted as dispersive shocklets, to the emergence of an unexpected global collective behaviour. The latter phenomenon is characterized by a strong non-homogeneous redistribution of the spatial fluctuations, whose description is provided by the NLSE and the LRVE, and unveils the formation of a giant shock singularity. From theoretical analysis [39], it turns out that - in the short-range regime - wave breaking occurs at random positions in the turbulent field, predominantly around high-amplitude fluctuations, leading to a gas of coherent dispersive shocklets in the midst of turbulent fluctuations. On the other hand, for highly nonlocal Kerr samples, the regularization of the global incoherent shock does not require the formation of a regular oscillating DSW structure because the self-organization of the turbulent waves ensemble makes the field oscillate as a whole. The momentum of the speckled beam [Eq. (31)] is radially outgoing and exhibits a shock-like singularity, while the envelope of the intensity of the beam experiences a ring-shaped collapse-like behaviour. The fluctuations of the incoherent wave then result to be pushed towards the annular shock front, which leaves behind itself an internal region of the beam with a high degree of coherence. In other terms, the dynamics is featured by a dramatic degradation of the coherence properties on the annular boundary of the beam, while its internal region exhibits a significant coherence enhancement.

Experimental observations of incoherent DSWs are reported in Sec. 3.4, together with related numerical simulations. Figure 15 illustrates results in quasi-local regime, in particular Figs. 15f-h show theoretically the occurrence of shocklets when nonlinear effects predominate. Same studies in highly nonlocal regime are in Fig. 16. Simulations of NLSE (Figs. 16g-i) and incoherent DSW peculiar profile is distinguishable at highest power. Another signature of DSW emergence is in the spectrograms in Figs. 16m-o, attained by LRVE simulations. At a linear regime (Fig. 16m) there is no evidence of any anomalous behavior. As the pump power increases, the spectrogram is affected by a Z-shaped distortion: the coherence length $\lambda_c \sim \Delta k^{-1}$ decreases at shock front (Δk_{shock} determines the boundaries of the admitted k values), and it increases in the internal region of the beam. This dynamics is conservative but irreversible, because the non-equilibrium thermodynamic condition is stabilized by an irreversible self-organization of the random waves.

3. Experimental Observations in Thermal Media

Shock waves described by Eq. (12) have been originally shown in an experiment from [27]. The sample is a cell of length 1mm filled with an aqueous solution of rhodamine B (RhB), with a concentration of 0.6mM. Measurements of the shock profiles are in Fig. 5. A Gaussian CW laser beam of intensity waist $W_0 = 20\mu\text{m}$, at wavelength $\lambda = 532\text{nm}$, propagates in a material with linear refractive index $n_0 = 1.3$, defocusing Kerr coefficient $n_2 = -7 \times 10^{-7}\text{cm}^2\text{W}^{-1}$, loss length $L_{loss}^{-1} = 62\text{cm}^{-1}$. For water

$D_T = 1.5 \times 10^{-7} \text{m}^2 \text{s}^{-1}$, $\rho_0 = 10^3 \text{kg m}^{-3}$, $c_p = 4 \times 10^3 \text{J kg}^{-1} \text{K}^{-1}$, $|\frac{\partial n}{\partial T}|_0 = 10^{-4} \text{K}^{-1}$. The degree of nonlocality is estimated as $\sigma = 0.3$.

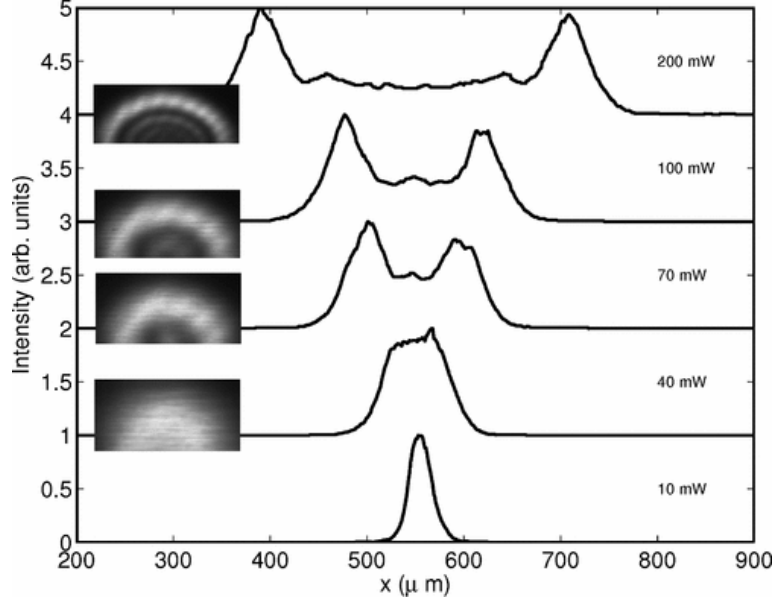


Figure 5. Experimental transverse intensity profiles of an initial Gaussian beam propagating in a thermal medium. Measurements are performed for varying input power $P = \pi W_0^2 I_0$. Insets show the 2D output patterns. FIG. 5 reprinted with permission from [27]. Copyright 2007 by the American Physical Society.

The beam exhibits, beyond the shock point, the formation of undular bores moving outward with increasing power. The next subsections report different experiments exhibiting DSWs in nonlocal samples.

3.1. Rhodamine and Time Asymmetric Quantum Mechanics Interpretation

In this section we report two experiments in order to validate the presence of GVs in DSWs: a 2D propagation pattern to observe GVs decay rates Γ_n [36], and a 1D experiment to show that GVs describe also the M-shaped profile in the far field of a DSW in HNA [38]. These are validations of TAQM in describing DSW propagation.

The experimental setup is illustrated in Fig. 6A. Samples are prepared by dispersing 0.1mM of RhB in water. The solution is placed in a cuvette 1mm thick in the propagation direction. The measured defocusing Kerr coefficient is $|n_2| = 2 \times 10^{-12} \text{m}^2 \text{W}^{-1}$ and the absorption length is $L_{loss} \simeq 1.6 \text{mm}$ at the laser wavelength 532nm [30]. The CW laser beam is focused through a lens into a sample. Light is collected by a spherical lens and a Charged Coupled Device (CCD) camera. A microscope is placed above the sample in order to capture top-view images of the laser beam along the propagation direction Z . The difference between the two experimental apparatus is the choice of the first lens (L1). In the 2D experiment [36], L1 is spherical with focal length 10cm, and a focus spot size of $10 \mu\text{m}$. The setup was placed having the beam propagating vertically through the sample, reducing thermal convection in the water. In the 1D experiment [38], authors used a cylindrical lens as L1, with focal length $f = 20 \text{cm}$ in order to mimic a nearly one-dimensional propagation. Being Z the propagation direction, the lens focuses the beam in the X direction. The input spot dimension is

1.0mm in the Y direction and $35\mu\text{m}$ in the X direction. These geometrical features make the one-dimensional approximation valid and allow us to compare experimental results with the theoretical one-dimensional model. The diffraction length in the X direction is $L_d = 3.0\text{mm}$. This time, the setup was placed horizontally.

Figures 6B,C report the observed laser beam propagation top-view, detected by a microscope through RhB fluorescence, and the numerical calculation from the NLSE, respectively. The beam displays the characteristic strongly defocusing and the M-shaped behavior, also evident in the transverse sections of the intensity in Figs. 6D,E. These are signatures of DSWs in nonlinear media at high power.

Decay rates in Fig. 7 are detected by slicing the intensity profile $I(X, Z)$ at $X \simeq 0.1\text{mm}$ (yellow line in Fig. 6B) and fitting the intensity versus Z with two exponential functions. Different power levels exhibit very different dynamics. The presence of double exponential decays, that is, the superposition of the first two GV's, is more evident at high power. It was observed and calculated that double-exponential decay dynamics obey the quantized spectrum scaling $\Gamma_2/\Gamma_0 = 5$ at all investigated power levels, as shown in Fig. 7D. This demonstrates that authors of [36] excited the fundamental state f_0^- and the first excited state f_2^- . Odd states are not excited, as expected from Gaussian TEM_{00} x -parity. Each of the two rates has a square root dependence on P , signature of the underlying nonlinearity. This power dependence distinguishes RHO dynamics from linear loss, due to absorption and scattering.

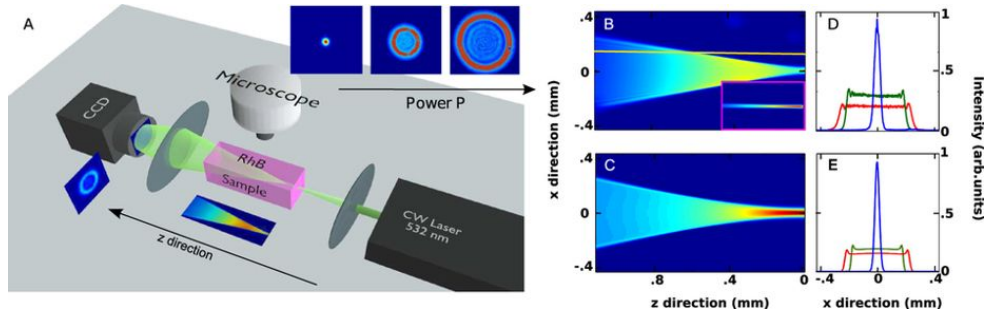


Figure 6. **A** Experimental setup. Authors of [36,38] collected the transmitted and fluorescence images of the laser beam propagating in RhB samples. Two types of launching lenses L1 were used: a cylindrical and a spherical, for the 1D and 2D experiments, respectively. The top fluorescence image of the propagating beam was collected by a microscope placed above the RhB samples. The second lens is spherical and was used to collect the transverse output profile. **B,C** Top-view intensity distribution as obtained from 2D experiment B and numerical simulations C. Respectively experimental **D** and numerical **E** sections of the images B and C taken at $z = 0.2$ (red), 0.6 (green) and 0.9mm (blue).

Reprinted by permission from Macmillan Publishers Ltd. from [36]. Copyright 2015.

The RHO eigenstates are quasi-eigenstates of the Fourier transform operator, which in optics represents the far field. Let us consider the RHO Hamiltonian in the momentum basis ($\hat{p} \rightarrow \mathbf{p}$ and $\hat{x} \rightarrow i\partial_{\mathbf{p}}$)

$$\hat{H}_{RHO}(\mathbf{p}, i\partial_{\mathbf{p}}) = \frac{\mathbf{p}^2}{2} + \frac{1}{2}\gamma^2\partial_{\mathbf{p}}^2 = -\hat{H}_{RHO}(-i\partial_x, x). \quad (33)$$

Pure GV's are unfeasible to describe a physical experiment, because one cannot neglect that GV's have an infinite support, i.e., the x -region where the eigenfunction is not null, is not finite. In order to account for the spatial confinement of the experiment,

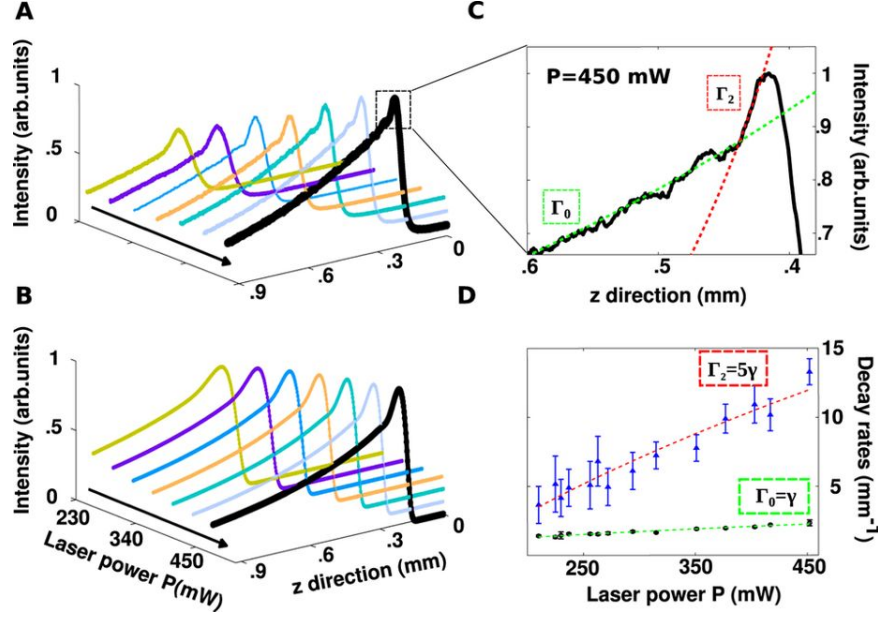


Figure 7. **A** Observed intensity decay at different laser powers, obtained by slicing along $X \simeq 0.1\text{mm}$ the top-view intensity distribution the propagation direction (see the yellow line in Fig. 6B). **B** Numerically calculated decays in the conditions of panel A. **C** Peak region of the experimental curve at $P = 450\text{mW}$. The superposition of the first two exponential decays unveils the presence of two GV's, the fundamental state, $n = 0$ (slowly decaying) and the first excited state, $n = 2$ (fastly decaying). **D** Decay rates vs P for the fundamental state, Γ_0 (filled circles) and the excited state, Γ_2 , (triangles). Reprinted by permission from Macmillan Publishers Ltd. from [36]. Copyright 2015.

authors of [38] introduced the windowed GV's:

$$\phi_G^W(x) = \sum_{n=0}^N \sqrt{\Gamma_n} f_n^- \langle f_n^+ | \psi(x, 0) \rangle \text{rect}_W(x), \quad (34)$$

where

$$\text{rect}_W(x) = \begin{cases} 0 & \text{for } |x| \geq W \\ 1 & \text{for } |x| < W \end{cases},$$

with W is the finite size of the physical system. During the evolution, the Gamow ground state has the lowest decay rate, i.e., $\gamma/2$. This allows to consider, in the long term evolution, only the fundamental GV, and so only the Fourier transform \mathcal{F} of the fundamental state of Eq. (34):

$$\begin{aligned} \tilde{\psi}(k_x) &= \mathcal{F} \left[f_0^-, W(x) \right] = \\ &= \left(\frac{1}{4} + \frac{i}{4} \right) e^{-\frac{ik_x^2}{2\gamma}} \frac{(-i\gamma\pi)^{1/4}}{W} \times \left\{ -\text{Erf} \left[\frac{(\frac{1}{2} - \frac{i}{2})(k_x - W\gamma)}{\sqrt{\gamma}} \right] + \text{Erf} \left[\frac{(\frac{1}{2} - \frac{i}{2})(k_x + W\gamma)}{\sqrt{\gamma}} \right] \right\}. \end{aligned} \quad (35)$$

Eq. (35) provides an analytical expression of the far field, which is compared below with the experiments. Indeed, Eq. (35) allows to predict in closed form the typical M-shaped shock profile: it describes the internal undular bores and the correct scaling of the undulation period with respect to the power, i.e. the period T is predicted to

scale with the square root of γ , and hence with the forth square root of the beam input power.

Figure 8 reports experimental results in RhB, through the previously described setup, and the comparison with the numerical results. Images of the beam in the far field (corresponding to the square modulus of the spatial intensity Fourier transform) for different input powers were collected and shown in Figs. 8a,b. For low power (not reported) the elliptical beam profile remains Gaussian along propagation. A different phenomenon occurs while increasing the power: the beam transverse section along X broadens and develops intensity peaks on its lateral edges. Essentially, it becomes M-shaped. These results are in remarkable agreement with Eq. (35), as shown in Figs. 8c,d.

Different positions in the Y direction correspond to different power levels. Any power level furnishes a different value of γ , being $\gamma = \sqrt{\frac{p}{\pi\sigma^2}}$. The Gaussian beam profile in the Y direction, that is, $p \propto \exp(-y^2)$, provides the link between Y , P and γ . This implies that, observing a CCD image, intensity profiles at different Y correspond to different powers. Therefore, the expected exponential trend with respect to the power can be extracted from a single picture by looking at different Y positions. Figure 8e exhibits a fitting with two exponential decays in an intensity profile versus power. The extracted ratio of the related two decay rates is 5 and hence in agreement with the expected quantized theoretical values described in Sec. 2.2.

Undular bores of DSWs were analyzed and exhibited in Fig. 8f, while the field intensity undulation period T versus P is shown in Fig. 8g. In order to demonstrate univocally that $T \propto \sqrt[4]{P}$, inset in Fig. 8g reports the period T as function of $\sqrt[4]{P}$. The resulting linear behavior confirms the theoretical results.

3.2. Nonlinearity and Disorder in Thermal Media

Thermal media have been investigated also in their interplay with disorder. Theoretical studies demonstrated that, even if solitons are stable under a certain amount of randomness, the latter competes with nonlinearity, while nonlocality filters disorder-induced scattering effects and soliton random walk can be efficiently suppressed in highly nonlocal media [50,52,82]. DSWs are nonlinear coherent oscillations, and the phenomenon of light scattering affects their formation in significant way [30].

In this section we report experiments in two different optical systems that combines third-order nonlinearity (high-power laser beams) with nonlocality (thermal material response) and disorder (scattering particles). The first thermal medium is a dispersion of silica spheres of $1\mu\text{m}$ diameter in 0.1mM aqueous solution of RhB. The second one is a $1\text{mm} \times 1\text{mm} \times 8.5\text{mm}$ parallelepiped of silica aerogel. Despite observations of DSWs in disordered thermal media, a theoretical model that comprehends both nonlinearity, nonlocality and disorder has been developed only for solitons [50]. The existing theoretical model for DSWs is summarized below and neglects the nonlocality contribution. It approximates thermal nonlinearity to a local Kerr effect, and adds a random potential [30].

We start from Eq. (12) with $\Delta n[|A|^2] = n_2|A|^2 + \Delta n_R(X, Y, Z)$ and $L_{\text{loss}} \sim \infty$ (no loss). Through the same scaling of Sec. 2.1 and approximation to cylindrical symmetry $\partial_y \sim 0$, we obtain

$$i\epsilon\partial_z\psi + \frac{\epsilon^2}{2}\partial_x^2\psi - |\psi|^2\psi + U_R\psi = 0, \quad (36)$$

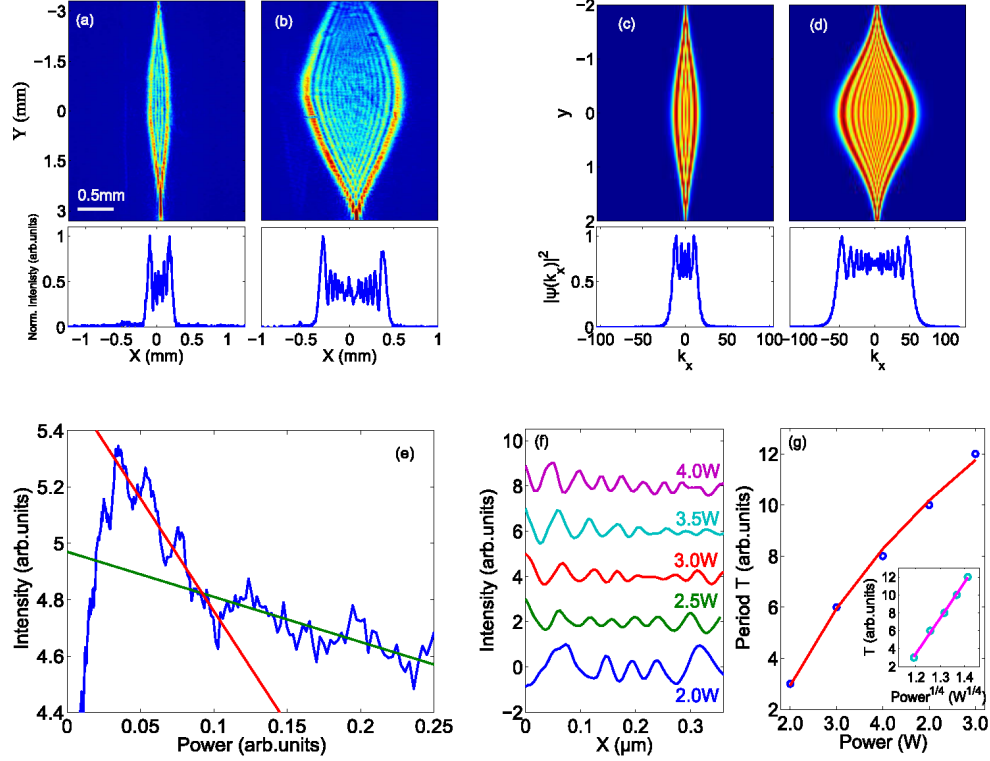


Figure 8. (a,b) CCD image of the light beam at laser powers $P = 2\text{W}$ and 4W , respectively; the bottom panels show the normalized intensity profile at the maximum waist along $Y = 0$. (c) Analytical solution obtained by Eq. (35) changing Gaussianly the power P in the y direction. (d) As in (c) but for higher powers; the bottom panels show the slice of panel (c) and (d) at $y = 0$, i.e., Eq. (35) square modulus for $W = 1.5$ and $\gamma \simeq 12$ and $\gamma \simeq 40$, respectively. (e) Log-scale normalized intensity as a function of power, as obtained by slicing along Y a region in panel (b). The slopes of the straight lines give the GV decay rates ($\gamma_1 = -8 \pm 0.4$ and $\gamma_2 = -1.6 \pm 0.1$). Their quantized ratio is 5.0 ± 0.4 as expected from theory [35]. (f) Intensity oscillations for different power values. (g) Measured oscillations period T as a function of power; continuous line is the fit function $T \propto \sqrt[4]{P}$, as expected by the theory; the inset shows the same curve of (g) with $P^{1/4}$ as abscissa axis. Reprinted with permission from [38]. Copyright 2016 Optical Society of America.

with $U_R(x, y, z) = \frac{\Delta n_R(X, Y, Z)}{n_2 I_0}$ taken as a random dielectric noise mainly acting on the phase [30]. In the hydrodynamic limit $\epsilon \sim 0$, the phase chirp behaves like a moving unitary mass particle [30]:

$$\frac{d^2 x}{dz^2} = -\frac{dU}{dx} + \eta_R, \quad (37)$$

with $U = \exp(-x^2/2)$ the deterministic potential for a Gaussian TEM_{00} given by the nonlinearity, and $\eta_R = -\frac{dU_R}{dx}$ a Langevin force with Gaussian distribution, such that $\langle \eta_R(z) \eta_R(z') \rangle = \eta^2 \delta(z - z')$ and $\eta = \sqrt{\left\langle \left(\frac{dU_R}{dx} \right)^2 \right\rangle} \simeq \sqrt{\langle (\Delta n_R)^2 \rangle} (n_2 |I_0|)^{-1}$ the disorder strength. Brackets $\langle \cdot \rangle$ denote the statistical average, and the dependence of η_R on x, y is neglected for stochastic independence and cylindrical symmetry, respectively, thus $\eta_R \simeq \eta_R(z)$.

Figure 9 shows trajectories $x(z)$ (Figs. 9a,b) and phase space (x, v) (Figs. 9c,d),

where $v = \frac{dx}{dz}$, respectively without ($\eta = 0$) and with ($\eta = 0.1$) disorder, the latter obtained by a stochastic Runge-Kutta algorithm [83,84]. In absence of disorder (Figs. 9a,c) the shock is signaled by the intersection of multiple trajectories $x(z)$ and, in the phase space, this corresponds to the induced wave breaking phenomenon, that is, the folding of the velocity profile into a multivalued function for increasing z . In presence of disorder, Figs. 9b,d, the particle-like dynamics tends to diffuse, as is evident from the related trajectories and phase space. Correspondingly, the propagation distance before the intersections is greater for the disordered case and the shock is delayed in the z direction.

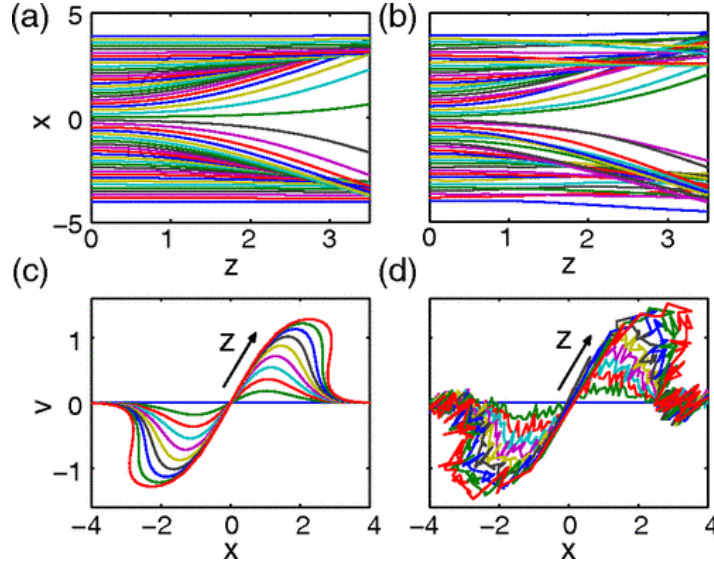


Figure 9. (a,b) Trajectories $x(z)$ and (b,d) phase space (x, v) , respectively with disorder strength $\eta = 0$ and $\eta = 0.1$. z varies from $z = 0$ to $z = 3$.

FIG. 4 reprinted with permission from [30]. Copyright 2012 by the American Physical Society.

We report here the experiments in RhB with silica spheres dispersions [30]. In order to vary the degree of disorder, several silica concentrations were prepared, ranging from 0.005w/w to 0.03w/w, in units of weight of silica particles over suspension weight. The experimental setup is similar to that illustrated in Fig. 6A. The first lens focuses the beam on the input face of the sample, reaching a beam waist $W_0 \simeq 10\mu\text{m}$. The aqueous solutions are put in $1\text{mm} \times 1\text{cm} \times 3\text{cm}$ glass cells with propagation along the 1mm vertical direction (parallel to gravity) to moderate the effect of heat convection. All measurements are performed after the temperature gradient has reached the stationary state and the particle suspensions are completely homogeneous. In [30], main loss mechanisms are absorption and scattering. The measured loss length (absorption plus scattering) varies in a range from 1.2mm to 1.6mm (highest value is for pure dye solution). These values are obtained by fitting with exponential decay the beam intensity vs propagation distance Z . The fact that the loss length is always greater than the position of the shock point [30] allowed authors to neglect losses at a first approximation in their theory. In addition, they found that the scattering mean free path is of the order of millimeters for all the considered samples. In Fig. 10 images of the transmitted beam on the transverse plane for different input laser powers P and various concentrations c are shown. The number and the visibility of the DSW oscillations increase with P and decrease with c , evidence of DSWs enhancement by

nonlinearity and inhibition by disorder.

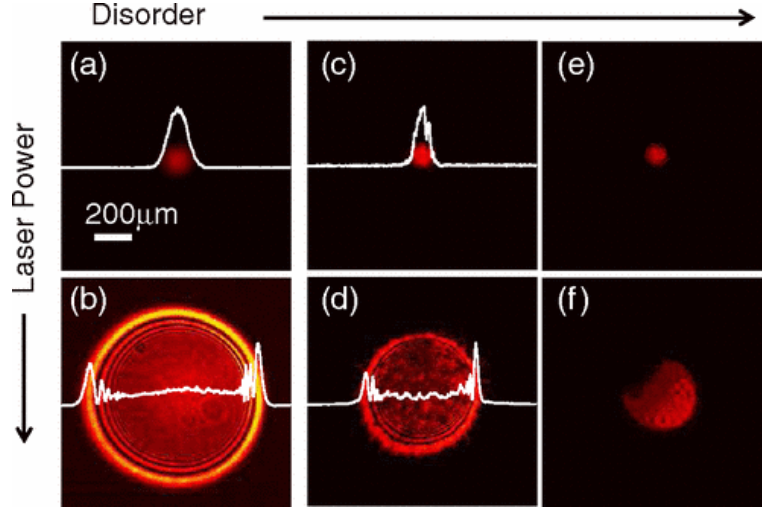


Figure 10. Transverse intensity patterns for different input power P and silica spheres concentration c : (a) $P = 5mW$, $c = 0w/w$, (b) $P = 400mW$, $c = 0w/w$, (c) $P = 5mW$, $c = 0.017w/w$, (d) $P = 400mW$, $c = 0.017w/w$, (e) $P = 5mW$, $c = 0.030w/w$, (f) $P = 400mW$, $c = 0.030w/w$. White 1D curves show the measured section of the intensity profiles vs X .

FIG. 10 reprinted with permission from [30]. Copyright 2012 by the American Physical Society.

Experimental observations have been also performed in silica aerogel [33]. The silica aerogel samples are prepared following a base-catalyzed sol-gel procedure [85], and in-depth details are given in [33]. It turns out that the sample used in the experiment has mass density $\rho = 0.215g/cm^3$ and refractive index $n_0 = 1.074$. Experimental setup is very similar to the previous ones (Fig. 1a), except for the sample. In [33], authors vary the input beam waist W_0 , the input laser power P_{in} , and record the transmitted intensity distribution $I(X, Y, Z = 8.5mm)$ by the CCD camera. Observations are shown in Fig. 11. Images in the second and third rows of Fig. 11 correspond to the same experimental conditions in term of incident laser power and beam size, but the incident laser beam impinges on different points. In correspondence of regions of the silica aerogel sample displaying low enough disorder (second row), a transition from scattering dominated regimes to nonlinear regimes is present: at moderate powers DSWs are not observed because of scattering losses, at high powers DSWs can be generated.

3.3. Dispersive Shock Waves in Biological Suspensions and Chemical Compounds

The study of optical effects in light propagation through chemical and biological solutions is a field of growing interest [34,40,54,86–89], both from a linear and a nonlinear perspective. However, although observations of nonlinear optical phenomena in chemical and soft-matter systems can be found in a large literature [27,30,32,33,36,38,46,54,90–93], and new experiments in chemical media are useful only if the material owns very specific properties, little is known about nonlinearity in biological fluids and the related literature is very recent [40,88]. Bio-materials can be very interesting, because both chemical and biological compounds can be excellent tunable thermal media, and DSWs were already observed [27,34,40].

For sake of completeness, in this section we report two experiments. The first one

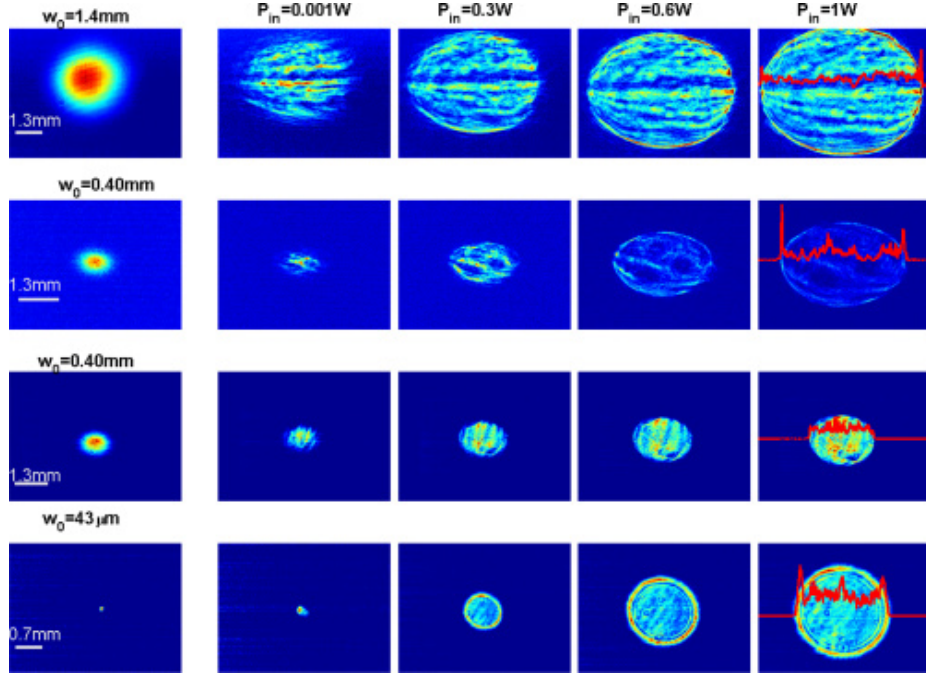


Figure 11. Far field intensity profiles at the output of the silica aerogel for P_{in} ranging from 1mW to 1W, and input beam waist w_0 ranging from $43\mu\text{m}$ to 1.4mm. Images in the second and third rows correspond to the same incident laser power and beam size, but different positions of the incident laser beam. Reprinted with permission from [33]. Copyright 2014 Optical Society of America.

in M-Cresol/Nylon, a chemical solution that exhibits an isotropic giant self-defocusing nonlocal nonlinearity, tunable by varying the nylon concentration [34]. The second one in human red blood cell suspensions, where the concentration of hemoglobin (Hb) and the input laser beam power make the nonlinearity change from self-focusing to nonlocal defocusing [40].

Figure 12 shows transverse profiles of output beam intensity after a propagation of 2mm in M-Cresol/Nylon. M-Cresol/Nylon is made up of an organic solvent (m-cresol) and a synthetic polymeric solute (nylon). When it is enlightened by a CW laser beam, light absorption induces local temperature variations, which reduces the refractive index, that is, the material experiences a nonlinear thermo-optical effect. In particular, [54]’s authors measured the M-Cresol/Nylon nonlinear Kerr coefficient n_2 and found that, if for pure m-cresol it is $-9 \times 10^{-8} \text{cm}^2/\text{W}$, for a nylon mass concentration of 3.5% it is $-1.6 \times 10^{-5} \text{cm}^2/\text{W}$, an order of magnitude higher than most of the other thermal nonlinear materials reported in literature. Authors generated the DSWs in Fig. 12 by focusing the input beam (a CW laser of wavelength 532nm) to $20 \pm 1\mu\text{m}$ onto the surface of M-Cresol/Nylon solution of 3.5% nylon concentration. The input laser power was varied ranging from $2\mu\text{W}$ to 20mW and, when it reached 5mW, the wave-breaking occurred.

Figure 13 reports a part of the results obtained in lysed human red blood cells aged samples, where free Hb determines sign and nonlocality of the optical nonlinearity from self-focusing (and self-trapping) to strong thermal defocusing effects, regime in which DSWs occur [40]. Beyond the biological issues related to human red blood cells, holding uncountable applications to life sciences and medicine, red blood cells refractive index tunability makes this medium be incredibly interesting also from a physical point of view [94–97]. In normal conditions, red blood cells are disc-shaped malleable cells,

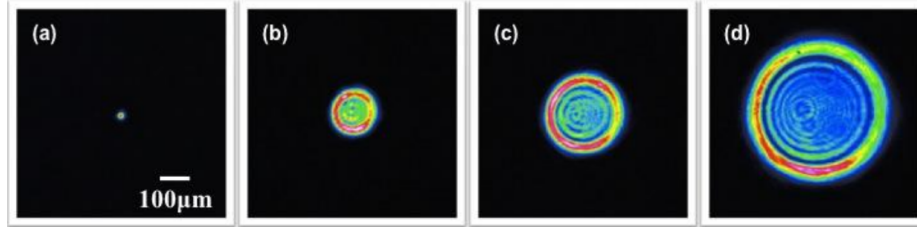


Figure 12. Output beam intensity transverse profiles, coming out from a 2mm long M-Cresol/Nylon solution. Input power varies: (a) $P_{in} = 2\mu\text{W}$, (b) $P_{in} = 5\text{mW}$, (c) $P_{in} = 10\text{mW}$, (d) $P_{in} = 20\text{mW}$. Reprinted with permission from [34]. Copyright 2014 Optical Society of America.

averagely with $8\mu\text{m}$ of diameter and $2\mu\text{m}$ of thickness, which have a spatially uniform refractive index because of the lack of nuclei and most organelles [95,97]. To enable the passage through veins and narrow microcapillaries, red blood cells exhibit distinctive deformability. Since their optical properties depend on the shape and refractive index of cells, they can be used as tunable optofluidic microlenses [96].

The red blood cell refractive index is mainly determined by Hb, which is the largest part of the erythrocyte dry content by weight [94]. Fig. 13a shows the output beam waist as a function of input power through the Hb solutions for four different concentrations, from 2.4 to 15.0 million cells per mL. Experiments in [40] are performed by using a linearly polarized CW laser beam with a wavelength of 532nm focused through a lens of 125mm focal length into a 3cm long glass cuvette filled with the red blood cell suspensions. In particular, the focused beam has initial waist $W_0 = 28\mu\text{m}$ at the focal point, which was located at 1cm away from the input facet of the cuvette to avoid heating and surface effects [88]. Outputs from the sample were monitored with a CCD camera and a power detector, and are reported in Figs. 13b-e, at variance of Hb concentration and input power. DSWs occur at high power (Figs. 13c,e), more visible in high Hb concentration regime (Fig. 13c).

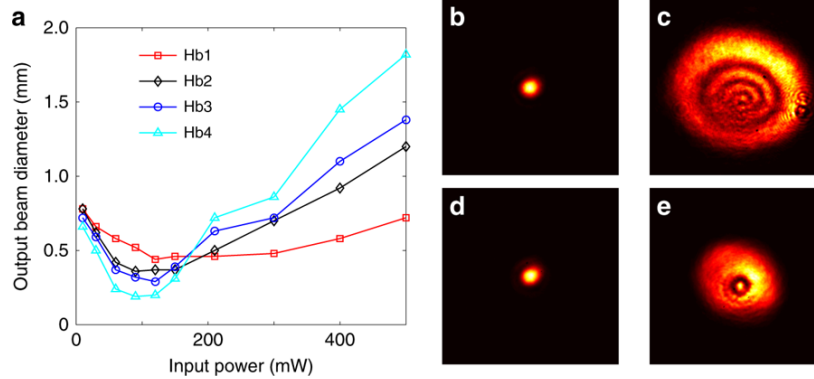


Figure 13. Output beam waist for varying Hb concentration and input power. **a** Detected beam diameter as function of input power through the Hb solutions for four different concentrations (Hb1-Hb4): 2.4, 5.1, 8.6, and 15.0 million cells per mL. Nonlinear self-focusing of the beam occurs around 100mW for high concentrations of Hb, but it subsequently expands into thermal defocusing rings at high powers. **b-e** Output beam transverse intensity profiles for **b** self-trapped beam at high concentration and low power, **c** DSW at high concentration and high power, **d** self-trapped beam at low concentration and low power, **e** DSW at low concentration and high power.

Reprinted by permission from Macmillan Publishers Ltd. from [40]. Copyright 2019.

3.4. Incoherent Dispersive Shock Waves

In this section, we report experimental evidence of incoherent DSWs theoretically introduced in Sec. 2.3. In particular, we show observations of the transition from shocklets to collective incoherent DSWs [37].

By varying the effective range of nonlocality, authors of [37] performed experiments both in the quasi-local and in the highly nonlocal regime. The experimental setup is sketched in Fig. 14. A CW laser ($\lambda = 532\text{nm}$) is made incoherent by passing through a 4-f telescope with a ground-glass plate in the middle. The initial coherence length $\lambda_c^0 \sim 200\mu\text{m}$, that is, the size of the speckles induced in the beam at the sample input face, is controlled by changing the waist impinging on the ground-glass plate. The sample is a dilute solution of methanol and graphene nanoscale flakes. The latter provide optimal conversion of absorbed laser energy into heat, thanks to the absence of fluorescence mechanisms and a negligible absorption. A CCD camera detects intensity images at the output.

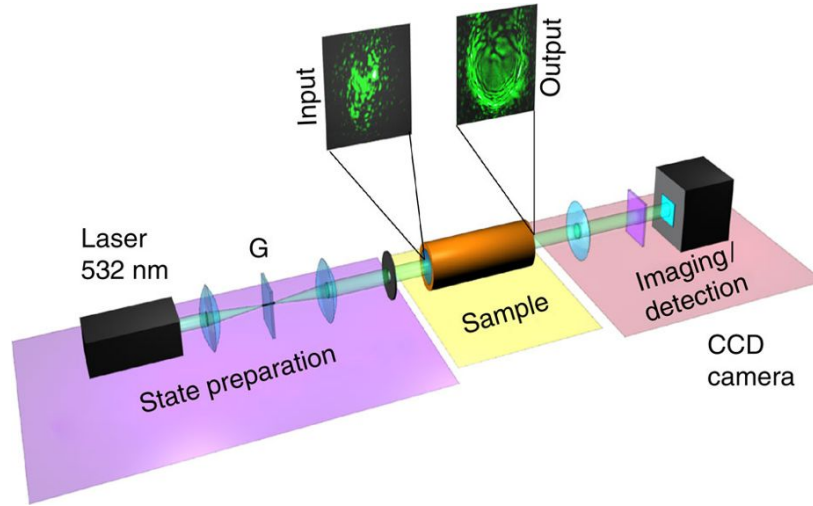


Figure 14. Experimental setup. A CW laser beam, $\lambda = 532\text{nm}$, is sent through a 4-f telescope. A ground-glass plate (G), placed in the midst of the telescope (on the focus of the first lens), generates a speckle pattern. The incoherent beam impinges the samples, a cylindrical tube filled with a solution of methanol and graphene nanoscale flakes, with waist $W_0 = 2.3\text{mm}$, while the initial coherence length λ_c^0 is controlled by changing the beam size on G. A CDD camera detects the output.

Reprinted by permission from Macmillan Publishers Ltd. from [37]. Copyright 2015.

Figure 15 shows the shocklets formation in a quasi-local regime. To reach this stage, concentration of graphene nano-flakes was increased, to increase the absorption and reduce the nonlocality, and a higher coherence length was chosen ($\lambda_c^0 \sim 250\mu\text{m}$), to inhibit collective behaviors. At low power (Fig. 15a for experiments, Fig. 15e for NLSE simulations) propagation is linear, so dominated by diffraction. As the input power increases (Fig. 15b for experiments, Fig. 15f for NLSE simulations), each speckle develops its own DSW, with a regular undular pattern. These is more evident in experimental (Figs. 15c,d) and numerical (Figs. 15g,h) zooms of shocklets undular bores.

Figure 16 reports the emergence of a giant collective incoherent DSW in highly non-local regime. Such a transition was made by decreasing the concentration of graphene nano-flakes and the coherence length ($\lambda_c^0 \sim 200\mu\text{m}$). At low power no collective behavior was observed, neither in the intensity profile (Figs. 16a,d for experiments, Fig. 16g

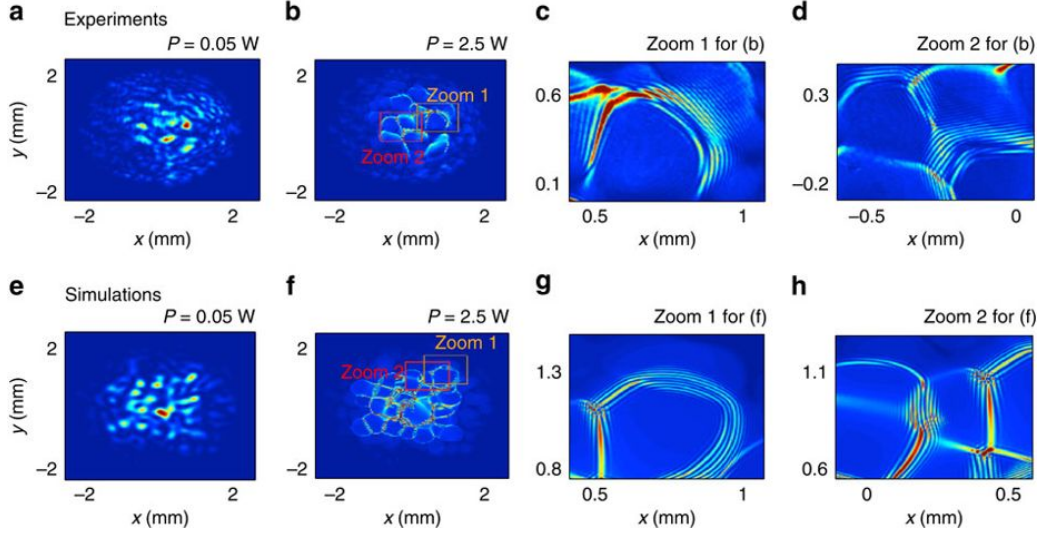


Figure 15. Experimental observation at short-range regime. **a,b** Experimental beam profiles of the output intensity recorded at power **a** $P = 0.05\text{W}$, **b** $P = 2.50\text{W}$. **c,d** Zooms on details of (b) that evidence the development of shocklets. **e,f** Numerical simulations of NLSE equation, and **g,h** corresponding zooms. Reprinted by permission from Macmillan Publishers Ltd. from [37]. Copyright 2015.

for NLSE simulations), nor in the spectrogram (Fig. 16j for experiments, Fig. 16m for LRVE simulations). At nonlinear regime, the occurrence of the annular reshaping of the beam is visible, with high frequencies piled on the boundaries, and low frequencies dominating the central part (Figs. 16b,c,e,f for experiments, Figs. 16h,i for NLSE simulations). The corresponding spectrograms show the Z-shape distortion, a signature of incoherent DSWs discussed in Sec. 2.3, and observable in Figs. 16k,l and Figs. 16n,o, respectively for experiments and simulations.

4. Conclusions

We reviewed the most widespread current theoretical models that describe nonlocal NLSE DSWs in spatial optical beam propagation. Moreover, we discussed their experimental observations.

In Sec. 2 the derivation of nonlocal NLSE was detailed, and main features of wave breaking in thermal Kerr media were reported [27]. In order to exhibit the theoretical interpretations of these phenomena as intrinsically irreversible, TAQM and turbulence wave theory approaches were summarized [11,37,39].

Section 3 is a collection of experiments on DSW generation in thermal media, first about a quite rich literature on observations in Rhodamine [27], and their TAQM explanation [35,36,38]. As second instance, we analyzed the interaction between disorder and nonlinearity in Rhodamine with silica spheres [30] and in silica aerogel [33], where the randomness inhibits the DSWs occurrence. Moreover, we reviewed very recent works on generation of photonic wave breaking in chemical [34] and biological solutions [40], fields where DSWs are emerging as surprising tools, useful for sensing and control of extreme phenomena. Finally, we showed emergence of giant collective incoherent shock waves from random wave propagation in highly nonlocal media [37].

The study of nonlinear optics in new materials, like soft matter and biological suspensions, is opening the way to a new branch of photonics. Many applications include,

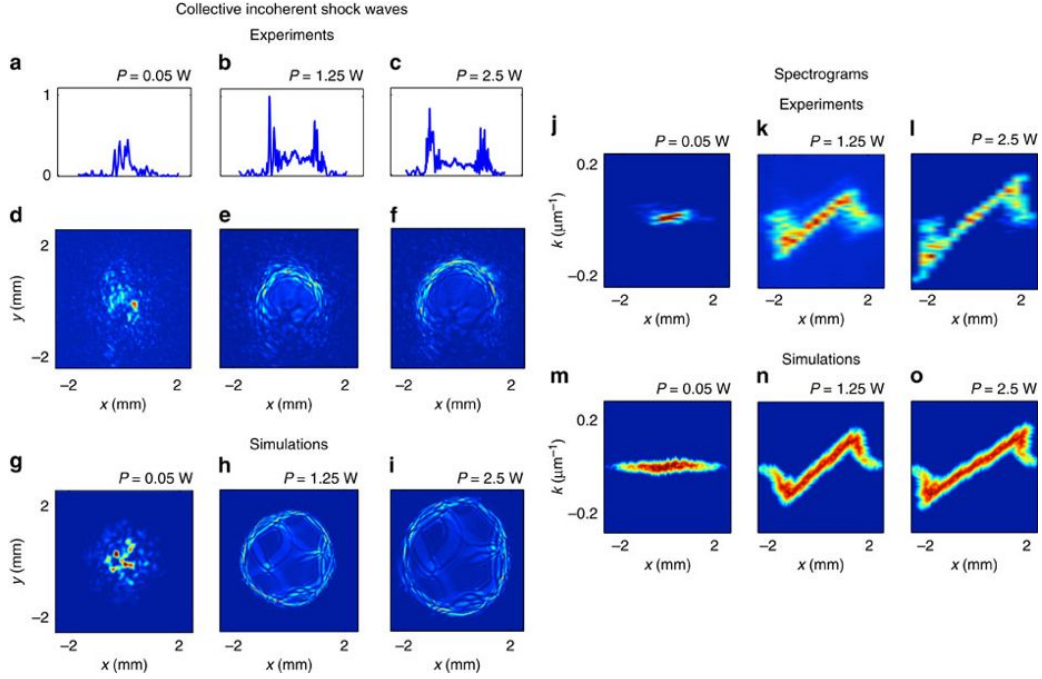


Figure 16. Experimental observation at long-range regime. **a-c** One dimensional intensity transverse profiles along x at $y = 0$. **d-f** Two dimensional intensity profiles. The asymmetry in the lower part of the beam is due to convection within the sample. **g-i** Numerical simulations of NLSE. **j-l** Experimental and **m-o** numerical spectrograms: the Z-shaped distortion reveals a dramatic coherence degradation on the annular boundaries of the beam (the coherence length decreases at the shock front), while a significant coherence enhancement occurs in the internal region of the beam. Input beam power: (a,d,g,j,m) $P = 0.05$ W, (b,e,h,k,n) $P = 1.25$ W, (c,f,i,l,o) $P = 2.50$ W.

Reprinted by permission from Macmillan Publishers Ltd. from [37]. Copyright 2015.

but are not limited to, spectroscopy, medicine, life sciences, non invasive diagnosis and time-resolved low-power probes. May the physics of nonlinear waves support the development of these new directions? Can novel mathematical tools deepen our understanding of nonlinear radiation-matter interaction? This manuscript is intended to sustain the improvement of theory and experiments concerning nonlinear optical propagation in highly nonlocal and complex matter.

We thank MD Deen Islam for the assistance in the laboratory. We acknowledge support from the QuantERA ERA-NET Co-fund 731473 (Project QUOMPLEX), H2020 project grant number 820392, Sapienza Ateneo, PRIN 2015 NEMO, PRIN 2017 PELM, Joint Bilateral Scientific Cooperation CNR-Italy/RFBR-Russia 2018-2020, and the National Key R&D Program of China (2017YFA0303800).

References

- [1] A. V. Gurevich and L.P. Pitaevskii. Nonstationary structure of a collisionless shock wave. *Sov. Phys. JETP*, 38:291, 1974.
- [2] G. B. Whitham. *Linear and Nonlinear Waves*. Wiley, New York, 1999.
- [3] G. A. El. Resolution of a shock in hyperbolic systems modified by weak dispersion. *Chaos*, 15:037103, 2005.
- [4] C. Barsi, W. Wan, C. Sun, and J. W. Fleischer. Dispersive shock waves with nonlocal nonlinearity. *Opt. Lett.*, 32:2930, 2007.

- [5] M. A. Hoefer and M. J. Ablowitz. Interactions of dispersive shock waves. *Physica D*, 236:44, 2007.
- [6] M. A. Hoefer, M. J. Ablowitz, and P. Engels. Piston dispersive shock wave problem. *Phys. Rev. Lett.*, 100:084504, 2008.
- [7] M. Crosta, S. Trillo, and A. Fratalocchi. The whitam approach to dispersive shocks in systems with cubicquintic nonlinearities. *New J. Phys.*, 14(9):093019, 2012.
- [8] M. Conforti, F. Baronio, and S. Trillo. Resonant radiation shed by dispersive shock waves. *Phys. Rev. A*, 89:013807, 2014.
- [9] A. Moro and S. Trillo. Mechanism of wave breaking from a vacuum point in the defocusing nonlinear Schrödinger equation. *Phys. Rev. E*, 89:023202, 2014.
- [10] G. A. El and M. A. Hoefer. Dispersive shock waves and modulation theory. *Physica D*, 333:11, 2016.
- [11] G. Marucci, M. C. Braidotti, S. Gentilini, and C. Conti. Time asymmetric quantum mechanics and shock waves: Exploring the irreversibility in nonlinear optics. *Ann. Phys.*, 529:1600349, 2017.
- [12] D. H. Peregrine. Calculations of the development of an undular bore. *J. Fluid Mech.*, 25:321, 1966.
- [13] R. J. Taylor, D. R. Baker, and H. Ikezi. Observation of collisionless electrostatic shocks. *Phys. Rev. Lett.*, 24:206, 1970.
- [14] N. F. Smyth and P. E. Holloway. Hydraulic jump and undular bore formation on a shelf break. *J. Phys. Ocean.*, 18:947, 1988.
- [15] J. E. Rothenberg and D. Grischkowsky. Observation of the formation of an optical intensity shock and wave breaking in the nonlinear propagation of pulses in optical fibers. *Phys. Rev. Lett.*, 62:531, 1989.
- [16] B. Wetzol, D. Bongiovanni, M. Kues, Y. Hu, Z. Chen, S. Trillo, J. M. Dudley, S. Wabnitz, and R. Morandotti. Experimental generation of riemann waves in optics: A route to shock wave control. *Phys. Rev. Lett.*, 117:073902, 2016.
- [17] B. Damski. Formation of shock waves in a bose-einstein condensate. *Phys. Rev. A*, 69:043610, 2004.
- [18] A. M. Kamchatnov, A. Gammal, and R. A. Kraenkel. Dissipationless shock waves in bose-einstein condensates with repulsive interaction between atoms. *Phys. Rev. A*, 69:063605, 2004.
- [19] V. M. Pérez-García, V. V. Konotop, and V. A. Brazhnyi. Feshbach resonance induced shock waves in bose-einstein condensates. *Phys. Rev. Lett.*, 92:220403, 2004.
- [20] T. P. Simula, P. Engels, I. Coddington, V. Schweikhard, E. A. Cornell, and R. J. Ballagh. Observations on sound propagation in rapidly rotating bose-einstein condensates. *Phys. Rev. Lett.*, 94:080404, 2005.
- [21] M. A. Hoefer, M. J. Ablowitz, I. Coddington, E. A. Cornell, P. Engels, and V. Schweikhard. On dispersive and classical shock waves in bose-einstein condensates and gas dynamics. *Phys. Rev. A*, 74:023623, 2006.
- [22] J. J. Chang, P. Engels, and M. A. Hoefer. Formation of dispersive shock waves by merging and splitting bose-einstein condensates. *Phys. Rev. Lett.*, 101:170404, 2008.
- [23] E. Bettelheim, A. G. Abanov, and P. Wiegmann. Nonlinear quantum shock waves in fractional quantum hall edge states. *Phys. Rev. Lett.*, 97:246401, 2006.
- [24] G. A. El, A. Gammal, E. G. Khamis, R. A. Kraenkel, and A. M. Kamchatnov. Theory of optical dispersive shock waves in photorefractive media. *Phys. Rev. A*, 76:053813, 2007.
- [25] L. Romagnani, S. V. Bulanov, M. Borghesi, P. Audebert, J. C. Gauthier, K. Löwenbrück, A. J. Mackinnon, P. Patel, G. Pretzler, T. Toncian, and O. Willi. Observation of collisionless shocks in laser-plasma experiments. *Phys. Rev. Lett.*, 101:025004, 2008.
- [26] M. D. Maiden, N. K. Lowman, D. V. Anderson, M. E. Schubert, and M. A. Hoefer. Observation of dispersive shock waves, solitons, and their interactions in viscous fluid conduits. *Phys. Rev. Lett.*, 116:174501, 2016.
- [27] N. Ghofraniha, C. Conti, G. Ruocco, and S. Trillo. Shocks in Nonlocal Media. *Phys. Rev. Lett.*, 99:043903, 2007.

- [28] W. Wan, S. Jia, and J. W. Fleischer. Dispersive superfluid-like shock waves in nonlinear optics. *Nat. Phys.*, 3:46, 2007.
- [29] C. Conti, A. Fratalocchi, M. Peccianti, G. Ruocco, and S. Trillo. Observation of a gradient catastrophe generating solitons. *Phys. Rev. Lett.*, 102:083902, 2009.
- [30] N. Ghofraniha, S. Gentilini, V. Folli, E. DelRe, and C. Conti. Shock waves in disordered media. *Phys. Rev. Lett.*, 109:243902, 2012.
- [31] J. Garnier, G. Xu, S. Trillo, and A. Picozzi. Incoherent Dispersive Shocks in the Spectral Evolution of Random Waves. *Phys. Rev. Lett.*, 111:113902, 2013.
- [32] S. Gentilini, N. Ghofraniha, E. DelRe, and C. Conti. Shock waves in thermal lensing. *Phys. Rev. A*, 87:053811, 2013.
- [33] S. Gentilini, F. Ghajeri, N. Ghofraniha, A. Di Falco, and C. Conti. Optical shock waves in silica aerogel. *Opt. Express*, 22:1667, 2014.
- [34] V. Smith, P. Cala, W. Man, and Z. Chen. Dark soliton attraction and optical spatial shock waves observed in m-cresol/nylon solutions. In *CLEO: 2014*, page FW3D.1. Optical Society of America, 2014.
- [35] S. Gentilini, M. C. Braidotti, G. Marcucci, E. DelRe, and C. Conti. Nonlinear gamow vectors, shock waves, and irreversibility in optically nonlocal media. *Phys. Rev. A*, 92:023801, 2015.
- [36] S. Gentilini, M. C. Braidotti, G. Marcucci, E. DelRe, and C. Conti. Physical realization of the glauher quantum oscillator. *Sci. Rep.*, 5:15816, 2015.
- [37] G. Xu, D. Vocke, D. Faccio, J. Garnier, T. Roger, S. Trillo, and A. Picozzi. From coherent shocklets to giant collective incoherent shock waves in nonlocal turbulent flows. *Nat. Commun.*, 6:8131, 2015.
- [38] M. C. Braidotti, S. Gentilini, and C. Conti. Gamow vectors explain the shock profile. *Opt. Express*, 24:21963, 2016.
- [39] G. Xu, J. Garnier, D. Faccio, S. Trillo, and A. Picozzi. Incoherent shock waves in long-range optical turbulence. *Physica D*, 333:310, 2016.
- [40] R. Gautam, Y. Xiang, J. Lamstein, Y. Liang, A. Bezryadina, G. Liang, T. Hansson, B. Wetzell, D. Preece, A. White, M. Silverman, S. Kazarian, J. Xu, R. Morandotti, and Z. Chen. Optical force-induced nonlinearity and self-guiding of light in human red blood cell suspensions. *Light: Sc. Appl.*, 8:31, 2019.
- [41] Clifford S. Gardner, John M. Greene, Martin D. Kruskal, and Robert M. Miura. Method for solving the korteweg-devries equation. *Phys. Rev. Lett.*, 19:1095, 1967.
- [42] G. Fibich. *The Nonlinear Schrödinger Equation*. Springer International Publishing, 2015.
- [43] C. A. Carter and J. M. Harris. Comparison of models describing the thermal lens effect. *Appl. Opt.*, 23:476, 1984.
- [44] O. Bang, W. Krolikowski, J. Wyller, and J. J. Rasmussen. Collapse arrest and soliton stabilization in nonlocal nonlinear media. *Physical Review E*, 66:046619, 2002.
- [45] M. Peccianti, K. A. Brzdakiewicz, and G. Assanto. Nonlocal spatial soliton interactions in nematic liquid crystals. *Opt. Lett.*, 27:1460, 2002.
- [46] C. Conti, M. Peccianti, and G. Assanto. Observation of optical spatial solitons in a highly nonlocal medium. *Phys. Rev. Lett.*, 92:113902, 2004.
- [47] Q. Guo, B. Luo, F. Yi, S. Chi, and Y. Xie. Large phase shift of nonlocal optical spatial solitons. *Phys. Rev. E*, 69:016602, 2004.
- [48] C. Rotschild, O. Cohen, O. Manela, M. Segev, and T. Carmon. Solitons in nonlinear media with an infinite range of nonlocality: First observation of coherent elliptic solitons and of vortex-ring solitons. *Phys. Rev. Lett.*, 95:213904, 2005.
- [49] A. I. Yakimenko, Y. A. Zaliznyak, and Y. Kivshar. Stable vortex solitons in nonlocal self-focusing nonlinear media. *Phys. Rev. E*, 71:065603, 2005.
- [50] V. Folli and C. Conti. Frustrated brownian motion of nonlocal solitary waves. *Phys. Rev. Lett.*, 104:193901, 2010.
- [51] V. Folli and C. Conti. Anderson localization in nonlocal nonlinear media. *Opt. Lett.*, 37:332, 2012.
- [52] F. Maucher, W. Krolikowski, and S. Skupin. Stability of solitary waves in random nonlocal

- nonlinear media. *Phys. Rev. A*, 85:063803, 2012.
- [53] V. Folli and C. Conti. Random walk of solitary and shock waves in nonlocal disordered media. *New J. Phys.*, 15(8):085026, 2013.
 - [54] V. Smith, B. Leung, P. Cala, Z. Chen, and W. Man. Giant tunable self-defocusing nonlinearity and dark soliton attraction observed in m-cresol/nylon thermal solutions. *Opt. Mater. Express*, 4:1807, 2014.
 - [55] A. Alberucci, C. P. Jisha, and G. Assanto. Breather solitons in highly nonlocal media. *ArXiv e-prints*, 2016.
 - [56] A. Bohm. Resonance poles and Gamow vectors in the rigged Hilbert space formulation of quantum mechanics. *J. Math. Phys.*, 22:2813, 1981.
 - [57] A. Bohm, M. Gadella, and G. B. Mainland. Gamow vectors and decaying states. *Am. J. Phys.*, 57:1103, 1989.
 - [58] C. G. Bollini, O. Civitarese, A. L. De Paoli, and M.C. Rocca. Gamow states as continuous linear functionals over analytical test functions. *J. Math. Phys.*, 37:4235, 1996.
 - [59] M. Castagnino, R. Diener, L. Lara, and G. Puccini. Rigged Hilbert spaces and time-asymmetry: the case of the upside-down simple harmonic oscillator. *Int. Jour. Theo. Phys.*, 36:2349, 1997.
 - [60] A. Bohm and N. L. Harshman. Quantum theory in the rigged hilbert spaces - irreversibility from causality. *Lect. N. Phys.*, 504:179, 1998.
 - [61] A. Bohm. Time asymmetric quantum physics. *Phys. Rev.*, A60:861, 1999.
 - [62] R. de la Madrid and M. Gadella. A pedestrian introduction to gamow vectors. *Am. J. Phys.*, 70:626, 2002.
 - [63] D. Chruściński. Quantum mechanics of damped systems. *J. Math. Phys.*, 44:3718, 2003.
 - [64] D. Chruściński. Quantum mechanics of damped systems 2. *J. Math. Phys.*, 45:841, 2004.
 - [65] O. Civitarese and M. Gadella. Physical and mathematical aspects of gamow states. *Phys. Rep.*, 396:41, 2004.
 - [66] G. Marcucci and C. Conti. Irreversible evolution of a wave packet in the rigged-hilbert-space quantum mechanics. *Phys. Rev. A*, page 052136, 2016.
 - [67] A. Picozzi. Towards a nonequilibrium thermodynamic description of incoherent nonlinear optics. *Opt. Express*, 15:9063, 2007.
 - [68] S. Can, J. Shu, C. Barsi, S. Rica, A. Picozzi, and J. W. Fleischer. Observation of the kinetic condensation of classical waves. *Nat. Phys.*, 8:470, 2012.
 - [69] A. Picozzi, J. Garnier, T. Hansson, P. Suret, S. Randoux, G. Millot, and D.N. Christodoulides. Optical wave turbulence: Towards a unified nonequilibrium thermodynamic formulation of statistical nonlinear optics. *Phys. Rep.*, 542(1):1, 2014.
 - [70] R. W. Boyd. *Nonlinear Optics*. Academic Press, 3rd edition, 2008.
 - [71] C. J. Wetterer, L. P. Schelonka, and M. A. Kramer. Correction of thermal blooming by optical phase conjugation. *Opt. Lett.*, 14:874, 1989.
 - [72] P. Brochard, V. Grolier-Mazza, and R. Cabanel. Thermal nonlinear refraction in dye solutions: a study of the transient regime. *J. Opt. Soc. Am. B*, 14:405, 1997.
 - [73] E. C. Kemble. A contribution to the Theory of the B.W.K. Method. *Phys. Rev.*, 48:549, 1935.
 - [74] A. W. Snyder and D. J. Mitchell. Accessible Solitons. *Science*, 276:1538, 1997.
 - [75] E. Celeghini, M. Gadella, and M. A. del Olmo. Applications of rigged hilbert spaces in quantum mechanics and signal processing. *J. Math. Phys.*, 57:072105, 2016.
 - [76] G. Gamow. Zur quantentheorie des atomkernes. *Z. Phys.*, 51:204, 1928.
 - [77] G. Gamow. The quantum theory of nuclear disintegration. *Nature*, 122:805, 1928.
 - [78] V. E. Zakharov, V. S. L'von, and G. Falkovich. *Kolmogorov Spectra of Turbulence I*. Springer-Verlag, 1992.
 - [79] A. C. Newell, S. Nazarenko, and L. Biven. Wave turbulence and intermittency. *Physica D*, 152-153:520, 2001.
 - [80] S. Nazarenko. *Wave Turbulence*. Springer-Verlag, 2011.
 - [81] A. C. Newell and B. Rumpf. Wave turbulence. *Ann. Rev. Fluid Mech.*, 43:59, 2011.
 - [82] Y. V. Kartashov, V. A. Vysloukh, and L. Torner. Brownian soliton motion. *Phys. Rev.*

- A, 77:051802, May 2008.
- [83] R. L. Honeycutt. Stochastic runge-kutta algorithms. i. white noise. *Phys. Rev. A*, 45:600, 1992.
 - [84] R. L. Honeycutt. Stochastic runge-kutta algorithms. ii. colored noise. *Phys. Rev. A*, 45:604, 1992.
 - [85] A. Venkateswara Rao and P.B. Wagh. Preparation and characterization of hydrophobic silica aerogels. *Mat. Chem. Phys.*, 53:13, 1998.
 - [86] P. Latimer. Light scattering and absorption as methods of studying cell population parameters. *Ann. Rev. Biophys. Bioeng.*, 11:129, 1982.
 - [87] A. Ashkin, J. M. Dziedzic, and T. Yamane. Optical trapping and manipulation of single cells using infrared laser beams. *Nature*, 330:769, 1987.
 - [88] A. Bezryadina, T. Hansson, R. Gautam, B. Wetzel, G. Siggins, A. Kalmbach, J. Lamstein, D. Gallardo, E. J. Carpenter, A. Ichimura, R. Morandotti, and Z. Chen. Nonlinear self-action of light through biological suspensions. *Phys. Rev. Lett.*, 119:058101, 2017.
 - [89] J. Dervaux, M. Capellazzi Resta, and P. Brunet. Light-controlled flows in active fluids. *Nat. Phys.*, 13:306, 2017.
 - [90] C. Conti, G. Ruocco, and S. Trillo. Optical spatial solitons in soft matter. *Phys. Rev. Lett.*, 95:183902, 2005.
 - [91] R. El-Ganainy, D. N. Christodoulides, C. Rotschild, and M. Segev. Soliton dynamics and self-induced transparency in nonlinear nanosuspensions. *Opt. Expr.*, 15:10207, 2007.
 - [92] E. Greenfield, J. Nemirovsky, R. El-Ganainy, D. N. Christodoulides, and M. Segev. Shock-wave based nonlinear optical manipulation in densely scattering opaque suspensions. *Opt. Expr.*, 21:23785, 2013.
 - [93] W. Man, S. Fardad, Z. Zhang, J. Prakash, M. Lau, P. Zhang, M. Heinrich, D. N. Christodoulides, and Z. Chen. Optical nonlinearities and enhanced light transmission in soft-matter systems with tunable polarizabilities. *Phys. Rev. Lett.*, 111:218302, 2013.
 - [94] John M. Steinke and A. P. Shepherd. Comparison of mie theory and the light scattering of red blood cells. *Appl. Opt.*, 27:4027, 1988.
 - [95] N. Ghosh, P. Buddhiwant, A. Uppal, S. K. Majumder, H. S. Patel, and P. K. Gupta. Simultaneous determination of size and refractive index of red blood cells by light scattering measurements. *Appl. Phys. Lett.*, 88:084101, 2006.
 - [96] L. Miccio, P. Memmolo, F. Merola, P. A. Netti, and P. Ferraro. Red blood cell as an adaptive optofluidic microlens. *Nat. Commun.*, 6:6502, 2015.
 - [97] R. Gautam, R. A. Dluhy, M. B. Marques, J. Y. Oh, and R. P. Patel. Characterization of Storage-Induced Red Blood Cell Hemolysis Using Raman Spectroscopy. *Lab. Med.*, 49:298, 2018.